Resolving the multi-temperature debris disk around γ Doradus with *Herschel*

by

Hannah Broekhoven-Fiene
B.Sc., Queen's University, 2009

A Thesis Submitted in Partial Fulfillment of the
Requirements for the Degree of

MASTER OF SCIENCE

in the Department of Physics & Astronomy

Resolving the multi-temperature debris disk around γ Doradus with *Herschel*

by

Hannah Broekhoven-Fiene
B.Sc., Queen's University, 2009

Supervisory Committee

Dr. Brenda Matthews, Co-Supervisor
(Department of Physics & Astronomy)

Dr. Sara Ellison, Co-Supervisor
(Department of Physics & Astronomy)

Dr. JJ Kavelaars, Departmental Member
(Department of Physics & Astronomy)

Supervisory Committee

Dr. Brenda Matthews, Co-Supervisor
(Department of Physics & Astronomy)

Dr. Sara Ellison, Co-Supervisor
(Department of Physics & Astronomy)

Dr. JJ Kavelaars, Departmental Member
(Department of Physics & Astronomy)

ABSTRACT

We present *Herschel* observations of the debris disk around γ Doradus (HD 27290, HIP 19893) from the *Herschel* Key Programme DEBRIS (Disc Emission via Bias-free Reconnaissance in the Infrared/Submillimetre). The disk is well-resolved with PACS at 70, 100 and 160 μm and detected with SPIRE at 250 and 350 μm. The 250 μm image is only resolved along the disk's long axis. The SPIRE 500 μm 3 σ detection includes a nearby background source. γ Dor's spectral energy distribution (SED) is sampled in the submillimetre for the first time and modelled with multiple modified-blackbody functions to account for its broad shape. Two approaches are used, both of which reproduce the SED in the same way: a model of two narrow dust rings and a model of an extended, wide dust belt. The former implies the dust rings have temperatures of $\sim$90 and 40 K, corresponding to blackbody radii of 25 and 135 AU, respectively. The latter model suggests the dust lies in a wide belt extending from 15 to 230 AU. The resolved images, however, show dust extending beyond $\sim$350 AU. This is consistent with other debris disks whose actual radii are observed to be a factor of 2 - 3 times larger than the blackbody radii. Although it is impossible to determine a preferred model from the SED alone, the resolved images suggest that the dust is located in a smooth

continuous belt rather than discrete narrow rings. Both models estimate that the dust mass is 6.7×10^{-3} $M_{\oplus}$ and that fractional luminosity is 2.5×10^{-5}. This amount of dust is within the levels expected from steady state evolution given the age of γ Doradus and therefore a transient event is not needed to explain the dust mass. No asymmetries that would hint at a planetary body are evident in the disk at *Herschel*'s resolution. However, the constraints placed on the dust's location suggest that the most likely region to find planets is within 20 AU of the star.

Contents

List of Tables

List of Figures

Acknowledgements

I would like to thank:

Brenda Matthews, for your endless patience, making opportunities attainable, always looking out for my best interests, and making more excited about astronomy every time I leave your office.

Stan Chisholm, for always believing in me, encouraging me, and inspiring me.

Lisa Glass and Robert Wasmann, for helping me in the hardest of times and being true friends.

Charli Sakari, for putting me back together again and for many useful discussions regarding astronomy — actually, regarding everything.

Monica Turner, for being my tech support.

Eric Tuttle & Grace Miyagawa, for showing me how to love Victoria and all those days in the park and mornings at Moka House.

The UVic astrograds and my friends, for providing much needed relief and comraderie.

Sarah, Grant and Hannah Pownall, for being the most cherished memory of mine for 2011, providing the exact company, atmosphere and discussions that I needed and deeply appreciate.

JJ Kavelaars, for being my guardian angel of office equipment.

Gary Berry, for your prompt and speedy assistance with all my IT needs and emergencies.

Andy Pon, James DiFrancesco, Kaushi Bandara, Lisa Glass, Stephen Gwyn and Ben for the many drives up and down the observatory hill.

Disks Journal Club, Star Formation Journal Club and Star Talk, for the many interesting discussions and presentations of current work in astronomy.

My Supervisory Committee, for your helpful questions, comments and feedback which improved this thesis.

Mark Booth and Laura Churcher, for your patience in describing and explaining the fundamentals of debris disks and their modelling.

Shadi Chitsazzadeh, for patiently taking me through the detection equation.

Grant Kennedy, for getting me started in the photospheric modelling of the Taurus brown dwarfs.

Charli Sakari & JC Passy, for proof-reading my thesis and providing many helpful comments and suggestions.

Canadian Space Agency, for funding DEBRIS research.

and to the many others that I have not mentioned who have constructively contributed to my education and life in Victoria.

Dedication

To my Mom, my Granny and my Uncle Kevin.

Co-Authorship

The data that are analyzed in this thesis are a part of the DEBRIS collaboration. Therefore some of the tasks, which are performed for the entire data set, were done by DEBRIS team members.

- Section 3.1 - **Bruce Sibthorpe** performed the *Herschel* data reduction.
- Section 3.1 - **Grant Kennedy** measured the noise in all DEBRIS maps. The noise measurements quoted in Table 3.1 come from that work.
- Section 3.2 - **Samantha Lawler** performed the re-reduction of *Spitzer* archival data for $\sim$150 DEBRIS targets, including γ Dor.
- Section 4.1 - **Grant Kennedy** did the photospheric modelling for all DEBRIS targets.
- Appendix A - **Bruce Sibthorpe** produced the different combinations of scan maps.

Chapter 1

Introduction

Stars are observed to be surrounded by material during many stages throughout their lifetime. Initially, they are born in clouds of gas and dust and form by accreting material from gas-rich disks. During their main-sequence (hydrogen core burning) lifetime, many are known to harbour planets and dusty disks. In later evolutionary stages (specifically the Asymptotic Giant Branch stage), stars produce dust as they eject it into their outer environments. Dying stars can be surrounded by layers or ejecta that they have blown off their surface (known as planetary nebula). Even when only a stellar core remains, it can be surrounded by dust or material it has accreted from a companion star. Following the evolution of circumstellar material is as important as studying the star itself to better understand the processes occurring at each stage.

We see that young stars form in clouds of gas and dust and that many stars harbour planetary systems which are composed of planets and disks. Our Solar System, for example, contains 8 planets, the Asteroid Belt lying between the orbits of Mars and Jupiter, and the Kuiper Belt of comets outside Neptune's orbit. We know that there are very massive objects in the Kuiper Belt that have sizes $\gtrsim$1000 km such as the dwarf planets: Pluto (d $\sim$ 2300 km), Eris (d $\sim$ 2300 km), Haumea (d $\sim$ 1400 km) and Makemake (d $\sim$1500 km). The recent wealth of extrasolar (outside the solar system) planet detections shows us that there is a rich diversity among planetary systems around other stars. A natural question to ask is how we get from the formation of stars in clouds of gas and dust to the arrangement of the planetary systems that we observe. The key to understanding this transition is through studying the evolution in the geometry, composition and mass of the matter that surrounds a star during its lifetime (see Figure 1.1).

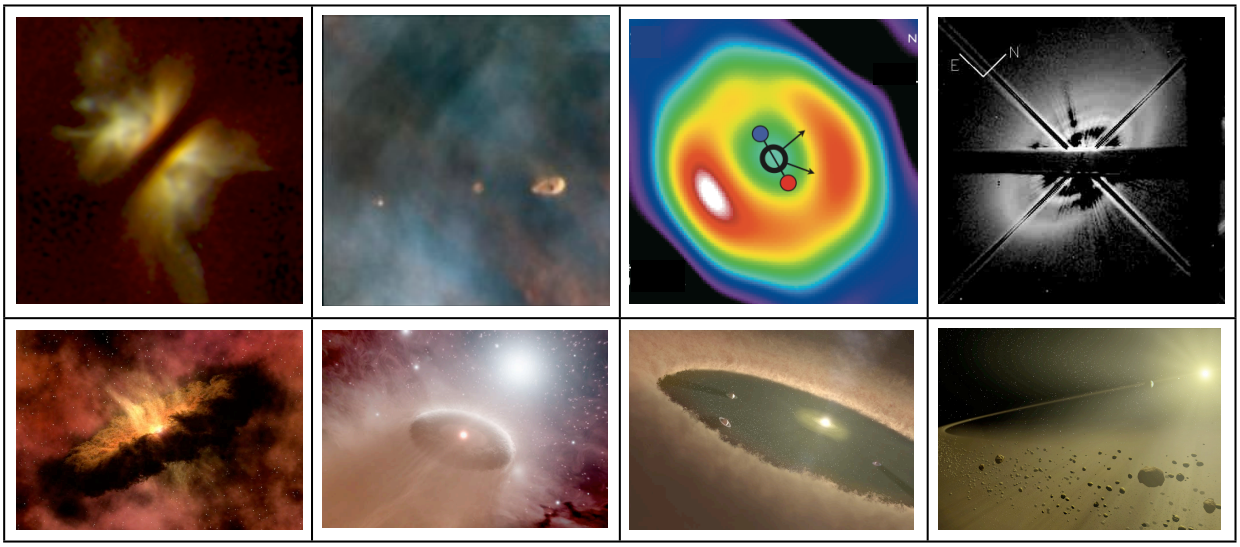

Figure 1.1 Different stages of circumstellar disks: (from left to right) a **protostellar accretion disk** which transports material onto the star, a **protoplanetary disk** where a planetary system is formed, a **transition disk** where the gas is being cleared out of the disk leaving behind a very gas-poor environment, and a **debris disk** where second generation dust is produced through collisions of large bodies in the planetary system. The top panels show actual observations of each phase and the bottom panels show artistic interpretations. References – (left to right) *top*: D. Padgett (IPAC/Caltech), W. Brandner (IPAC), K. Stapelfeldt (JPL) and NASA/ESA; Figure 4 of SR 21 from Pontoppidan et al. 2008; Figure 2 of HD 141569 from Mouillet et al. 2001. *bottom*: NASA/JPL-Caltech/R. Hurt (SSC); NASA/JPL-Caltech/T. Pyle (SSC); NASA/JPL-Caltech/T. Pyle (SSC); NASA/JPL-Caltech/T. Pyle (SSC).

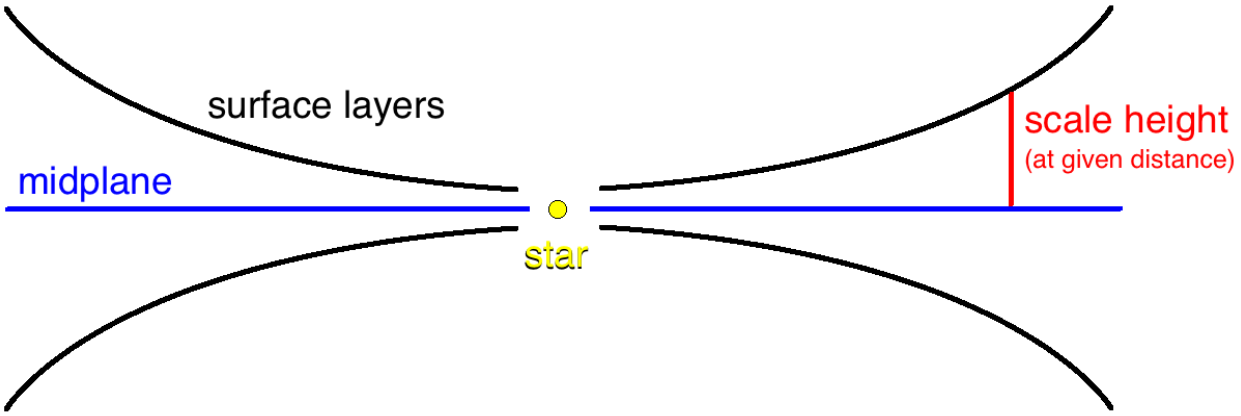

Figure 1.2 The basic geometry of an edge-on accretion disk (either protostellar or protoplanetary) showing the star at the centre *(yellow)*, the surface layers *(black)*, the midplane *(blue)* and the scale height *(red)*. Note that the scale height varies with distance from the star as the disk has a flared geometry.

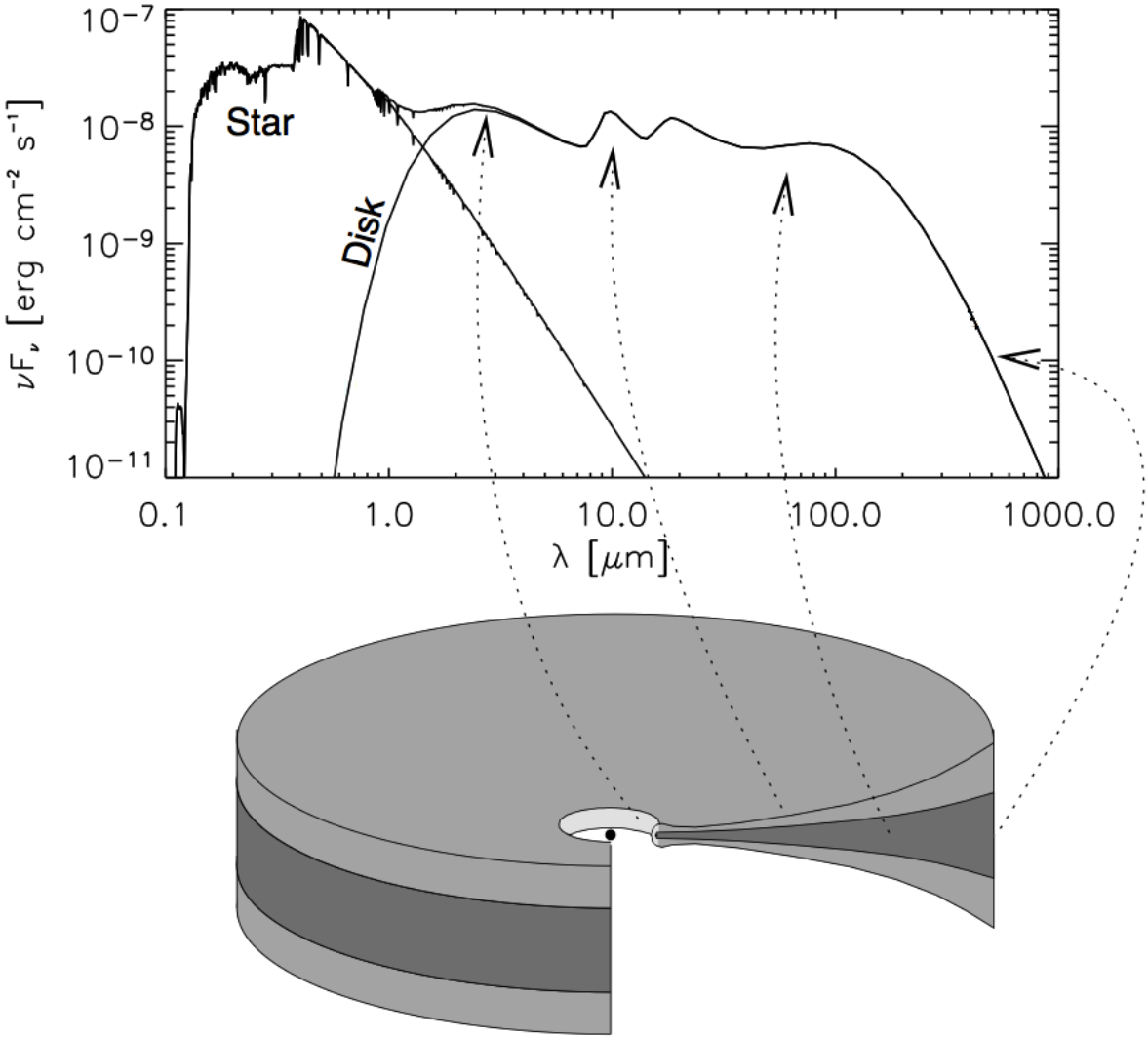

Figure 1.3 Figure 2 from Dullemond et al. (2007) showing the different regions of material in a protoplanetary accretion disk and their effect on the appearance of the SED of the star and disk system. The dust closest to the star *(light grey)* is the hottest. The warm surface layers *(medium grey)* shield the cool midplane *(dark grey)*.

Table 1.1. Abbreviations and acronyms

Abbreviation/ acronym	Name
DEBRIS	Disc Emission via Bias-free Reconnaissance in the Infrared/Submillimetre
DUNES	DUst around NEarby Stars
FWHM	Full Width at Half Maximum
HIFI	Heterodyne Instrument for the Far Infrared
IR	InfraRed
IRAS	InfraRed Astronomical Satellite
JCMT	James Clerk Maxwell Telescope
MIPS	Multiband Imaging Photometer for *Spitzer*
PACS	Photoconductor Array Camera and Spectrometer
PR drag	Poynting-Roberston drag
PSF	Point Spread Function
SCUBA	Submillimetre Common User Bolometer Array
SCUBA-2	Submillimetre Common User Bolometer Array 2
SED	Spectral Energy Distribution
SPIRE	Spectral and Photometric Imaging REceiver
submm	submillimetre

The protostar (a star in the process of forming) is initially surrounded by material known as a circumstellar envelope (Shu et al., 1987; Hartmann, 1998). The material that is accreted onto the protostar must lose angular momentum by the time it reaches the slowly rotating protostar since it originates from far distances ($\sim$ 1 pc or 31 trillion km). In order to conserve angular momentum during the accretion process, a circumstellar disk forms. At this stage in the disk's evolution, the disk is called a *protostellar accretion disk*. It is through this disk that the mass of the envelope accretes onto the protostar. The protostellar accretion disk (Figure 1.1), much like the cloud that contains it, is composed mostly of gas with comparatively little dust. (There is $\sim$100 times more gas than dust in the disk by mass.) Figure 1.2 shows the basic geometry of an accretion disk. The cut through the vertical centre of the disk is called the disk midplane. The extent of the disk above the midplane increases at further distances from the star, so that the disk is very thin near the star and quite thick in the outer regions giving the surface a bowled shape. Because of this shape the top layers of the disk are warmed by the star and they shield the midplane that consequently remains cool.

The circumstellar disk enters the next phase as the accretion of material onto the star slows and the main role of the disk turns to the formation of planetary systems. The structure of the disk remains the same and it is referred to as a *protoplanetary accretion disk* (see Figure 1.3 for the basic temperature structure of a protoplanetary accretion disk). The sizes of the dust grains can grow as the dust settles to the cooler midplane and the grains collide and stick. Solids can begin to agglomerate from micron sizes to larger bodies like pebbles, rocks, planetesimals and planets (Beckwith et al., 2000).

The gas-rich protoplanetary disk phase is completed by about $\sim$10 Myr after the birth of the star. The disk then enters the *transition disk* phase and the gas begins to leave the system. Much of the dust must also leave since the dust mass is observed to decrease by an order of magnitude (Wyatt, 2008). It is believed that the gas is cleared from the inside out since observations show gaps or holes in disks close to the star (Strom et al., 1989; Brown et al., 2007; Hughes et al., 2010; Andrews et al., 2011).

Once the gas is cleared out, the planetary system is revealed. If it contains massive objects like planets and planetesimals $\gtrsim$ 1000 km it will have the ingredients necessary to form a *debris disk*. The observed dust is a result of collisions between the planetesimals and thus debris disks are also referred to as second-generation disks.

These large objects determine the evolution of the debris disk; the location of the planetesimals determines the location of the dust and planets can alter the shape the disk.

Studying circumstellar disks of all ages reveals information about the formation and evolution of stars and their planetary systems. The environments in protostellar and protoplanetary disks (disks around young objects) influence the processes involved in the formation and evolution of protostars and protoplanets and disks observed around older main-sequence stars continue to carry clues about the processes involved.

1.1 Debris disks

The term debris disk is used to describe disks that contain bodies ranging from dust grains (down to submm sizes) to larger bodies (like pebbles and rocks) and planetesimals (up to $\gtrsim$1000 km). The Solar System's debris disk is comprised of the Asteroid Belt, the Kuiper Belt, other comets, Pluto and the other dwarf planets (everything except the eight planets and their satellites).

Debris disks provide another avenue to study of the formation and evolution of planetary systems. For example, in our own Solar System, the dynamics of bodies in our debris disk provides evidence that the Kuiper Belt probably formed *in situ* in a relatively quiescent environment (Parker et al., 2011, in press). Before debris disks and their implications on the planetary systems that contain them can be understood, there are some debris disk fundamentals which need to be described.

1.1.1 Origin of the dust

The dust in a debris disk is not remnant dust from the protoplanetary disk phase (i.e., dust that was not cleared out with the gas). Dust can only orbit the star for so long before it is removed from the system (see Section 1.1.2). Its lifetime in the disk is much shorter than the ages of the stars known to harbour debris disks (Backman & Paresce, 1993). This means that the dust must have been produced recently. Furthermore, since dust is observed around many stars with ages up to a few Gyr, it is unlikely that the dust in all these systems is due to recent transient events and more likely that it is continually replenished throughout a steady evolution.

The debris is produced in collisions amongst larger bodies that were formed at

earlier times in the disk. Thus protoplanetary disks set the stage for the formation and evolution of debris disks. The very presence of a debris disk implies that the planetary system formed large enough bodies to collide and produce such substantial amounts of dust. Furthermore, objects with sizes $\gtrsim$ 1000 km are needed to stir the material and initiate collisions within the disk (Kenyon & Bromley, 2004). This sets up a collisional cascade where larger bodies are ground down into smaller bodies and eventually into submicron-sized dust.

1.1.2 Location of the dust

The location of the dust is determined by the location of the planetesimals responsible for the dust-producing collisions. For the majority of debris disks, it is sufficient to describe the dust as being contained in a single ring (see the discussion in Wyatt 2008). However, there are systems which require the existence of multiple components to explain the observations (e.g., HR 8799: Su et al. 2009, ϵ Eridani: Reidemeister et al. 2011, HD 107146: Ertel, S. et al. 2011, HD 181327: Schneider et al. 2006). This leads to the interpretation that there can be more than one planetesimal belt; similar to the solar system which has an inner belt (the Asteroid Belt) and an outer belt (the Kuiper Belt), that are separated by planets that clear small bodies out of their orbits.

As small grains are produced, they are removed from the system by either radiation pressure or Poynting-Robertson drag[1] (hereafter PR drag, Burns et al., 1979). Radiation pressure is due to the stellar radiation pushing on the dust grain causing the eccentricity of its orbit to increase so that it travels further from the star (see description in Krivov, 2010). Smaller grains are more sensitive to it, since they have less gravitational force binding them to the system, and dust grains smaller than the "blowout size" are removed from the system completely. PR drag is also due to the central star's radiation; however, it causes dust grains to lose angular momentum and to spiral into the star.

For many of the disks with multiple dust components listed above, there is evidence that dust has been transported to other regions by radiation pressure or PR drag. The radiation profile of the dust component at 100-200 AU from HD 181327 is consistent with it being blown out by radiation pressure (Schneider et al., 2006); there is a

[1]Stellar wind drag can also contribute to dust removal around late-type stars (Plavchan et al., 2005).

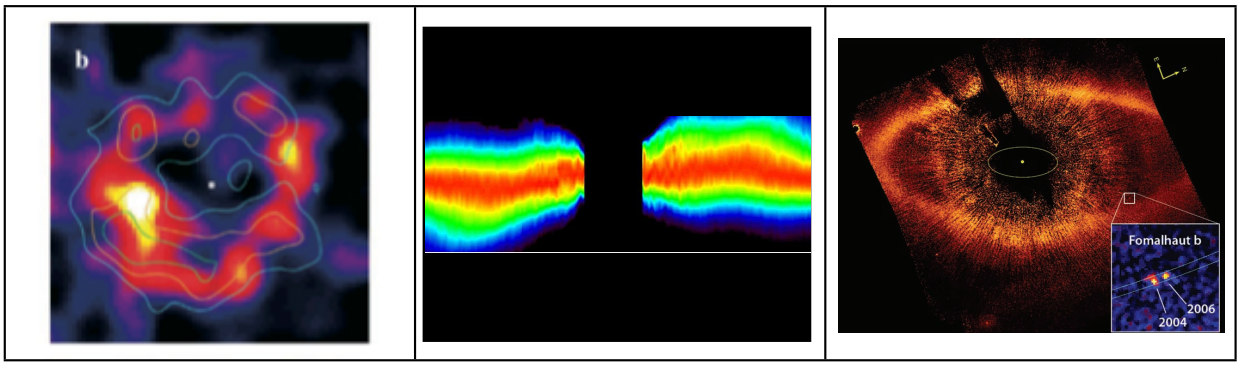

Figure 1.4 A planet can create features in the disk that are observable through the structure of the dust. Some examples include (left to right) clumps (face-on ϵ Eridani disk: Greaves et al., 2005), warps (edge-on β Pictoris disk: *credit: Sally Heap GSFC/NASA*) and sharp edges and offsets of the disk from the star (Fomalhaut: Kalas et al., 2008). See text for a description.

halo of small grains around HR 8799 thought to have been transported outwards (Su et al., 2009); and the ϵ Eridani system displays evidence of the dust being transported inwards (Reidemeister et al., 2011).

1.1.3 Structure of the dust

Planets can shape the dust distribution by creating either features in the radial distribution or asymmetries in the disk. The fate and location of the dust is ultimately determined by the system of larger bodies around it. Some examples of observable features that provide evidence of planets are shown in Figure 1.4:

Clumps: Large bodies can create resonances in the dust structure that appear as clumps. Such substructure has been observed in ϵ Eridani disk (Greaves et al., 1998, 2005).

Warps: A planet on an inclined orbit can produce a warp in the disk. The presence of a planet was inferred from the warp in the disk around β Pictoris (Mouillet et al., 1997; Augereau et al., 2001) and later confirmed by direct imaging (Lagrange et al., 2009, 2010).

Sharp edges: Planets orbiting just inside or just outside a dust ring can sharpen the edge of its radial profile. They can also clear out the regions between dust components. The profile of the edge of a disk can be used to place constraints

on a planet's mass and orbital parameters (as was done for a planet orbiting Fomalhaut: Quillen, 2006).

Offsets: A planet on an eccentric orbit can produce an offset between the disk's centre and the location of the star. For example, such an offset of 15 AU in the Fomalhaut system along with the sharp inner edge of the radial profile was used to predict the presence of a planet in orbit (Kalas et al., 2005) which was later confirmed by direct imaging (Kalas et al., 2008).

1.1.4 Properties of the dust

The dust produced in a debris disk can have sizes from 0.1 μm to 1 mm. The size distribution depends on the production mechanism and determines the slope of the Spectral Energy Distribution (SED) (Section 1.2.1) of the disk at submm wavelengths. The smallest sizes present depend on the properties of the host star that determine the dominant removal mechanisms (Section 1.1.2).

There are numerous dust compositions that can be explored in debris disks with different shapes, such as amorphous and crystalline. Silicates (Laor & Draine, 1993) are often used to model realistic dust grains (as opposed to dust grains that act like perfect blackbodies) although evidence of icy grains has also been found in certain disks (e.g., HD 181327: Chen et al. 2008). Different sized dust grains can be studied for a given composition as well. For instance, Su et al. (2009) investigate silicates with sizes between 0.5 and 10 μm. Spectra of dust in a debris disk are particularly useful for investigating the composition if they contain features that can be compared to those of spectra of dust grains measured in the laboratory, or spectra of cometary or asteroidal dust (e.g. Chen et al. 2006). These spectral features only appear if small dust grains are present in the system.

1.2 Detecting debris disks

Studying extrasolar debris disks requires a different approach than that used to study the Solar System's debris disk. In the Solar System, the large bodies (the dwarf planets, the asteroids, the Kuiper belt objects, etc.) are observable because they reflect sunlight, and they are close enough that their temperatures can be measured from submm observations. We cannot observe all the dust our debris disk contains because we are within the system. Conversely, in extrasolar systems the larger bodies

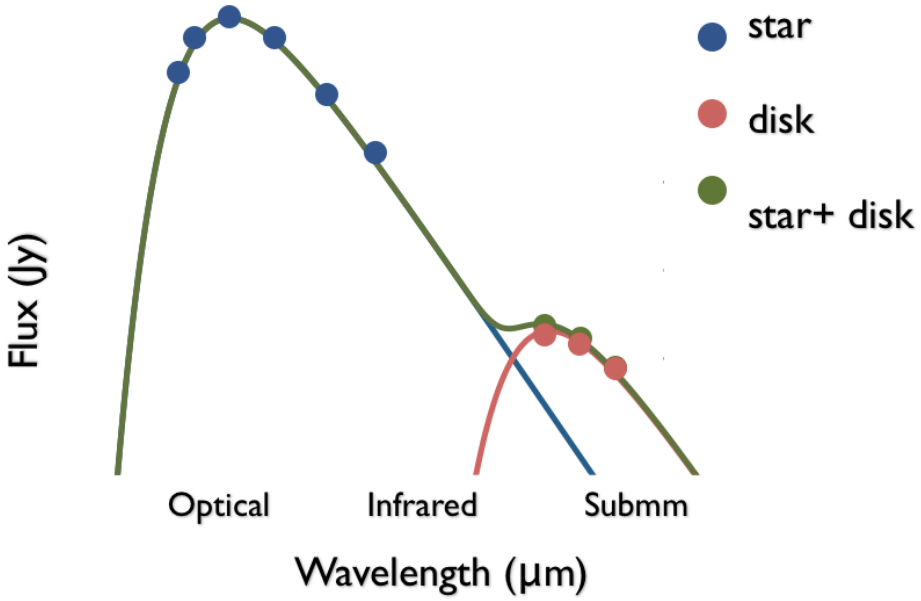

Figure 1.5 A cartoon SED of a star and disk system *(green)*. Optical fluxes are used to fit a photospheric model to the star *(blue)*. The expected photospheric fluxes in the infrared and submillimetre are subtracted from the observed fluxes to model the dust emission *(red)*.

are invisible to us and the dust renders the disk observable. We approach the study of an extrasolar debris disk by observing the amount, location and distribution of dust to infer the presence of the larger bodies that produce, place and shape it.

The dust is heated by the central star and so emits thermally. Small dust grains will also scatter starlight. The dust can therefore be observed at shorter wavelengths (optical and near-IR) through observations of scattered light and/or at longer wavelengths (mid-IR, far-IR, submm, mm) where the dust's thermal emission is brightest. The dust's thermal emission can be studied through spatially unresolved or resolved observations at these longer wavelengths as the emission contrasts well against the star's declining brightness. However, observations of scattered light require resolved imaging to distinguish it from the star whose emission peaks at these shorter wavelengths.

1.2.1 Unresolved studies

Debris disks were first identified with spatially unresolved SEDs. Observations with the Infrared Astronomical Satellite (*IRAS*) in the mid- to far-infrared revealed that

Vega, β Pictoris and Fomalhaut were unexpectedly bright in this wavelength range (Aumann et al., 1984). Many main-sequence stars were then observed to have an "IR excess" (see Figure 1.5), including γ Doradus. This is still the general approach used today to detect debris disks. The observations of a star in optical and near-infrared (blue points in Figure 1.5) are used to fit a photospheric model (blue line in Figure 1.5). The excess emission above the photosphere (hereafter just excess) due to dust (red points in Figure 1.5) is determined by subtracting off the predicted photospheric flux from the observed flux. (See Chapter 2 for an example of how unresolved fluxes are used to model the dust in an accretion disk.)

The simplest approach is to fit the excess emission with a blackbody function. This assumes that the dust is contained in a narrow ring at a single radius. Variations and modifications can be incorporated if necessary to explain additional features, such as a steeper decline in the SED at submm wavelengths. Estimates of the temperature and the luminosity of the dust come directly from the fitted blackbody function. The fractional luminosity, $f = L_{dust}/L_*$, is often used to compare debris disks to each other, where L_{dust} is the luminosity of the dust and L_* is the luminosity of the star.

If the SED is not well fit by a single blackbody function because the shape of the SED is too broad, it can be modelled with multiple narrow rings (fit with two or more blackbody functions) or an extended/wide disk (typically described by power-law surface density and power-law temperature distributions).

Observed fluxes at a given wavelength (or frequency, ν) are related to the dust mass by adopting an opacity relation, κ_ν. This relation is best understood at submm wavelengths. The dust must be optically thin at the wavelength of the observed flux that is used to measure the mass. This means that the dust emission that we observe has not been absorbed and re-emitted by other dust grains. In an accretion disk, for example, the dust is optically thick in the infrared where the emission from dust grains deeper in the disk has been absorbed and re-emitted many times by other grains before it makes its way out of the disk and is observed. Therefore submm observations, where the dust is optically thin in an accretion disk, must be used. The dust in debris disks, on the other hand, is optically thin across all wavelengths and so submm fluxes can be extrapolated from the model to be used in the opacity relation.

There are often a lot of (sometimes simplistic) assumptions that are used to derive the disk properties from the SED of the dust. First of all, realistic grains do not emit like perfect blackbodies. Although the SED can be modelled with realistic grains, often the SED is not sampled well enough to place meaningful constraints on

the composition. Spectroscopy can be used to identify spectral features which can constrain the composition of the dust (e.g., Chen et al., 2006) and the sizes of the grains. The very presence of spectral features indicates that the dust is composed of small grains as spectra of larger grains more closely resemble that of a blackbody.

Assuming a model for dust grains allows an estimate the disk size. A first approach is to assume that the dust grains emit like perfect blackbodies. This typically underestimates the size of the disk because realistic dust grains are inefficient at re-radiating the energy that they absorb. Therefore at the same distance from the star, they will be hotter than the blackbody temperature. (This effect depends on the grain's composition and size.) Therefore, the dust may actually be 2-3 times further from the host star than the blackbody radius suggests (Schneider et al., 2006; Matthews et al., 2010). Calculating the blackbody radius is still helpful, however, because it provides a parameter that can be easily used to compare disks to each other. When we compare the blackbody radii of different disks, we are actually comparing the temperatures of the disks in relation to the luminosity of the host star.

There are assumptions that go into the opacity relation, κ_ν, that is used to determine the disk mass. However, because the same opacity is used for many different disks, it gives a method to compare the cross-sectional area of different disks in a systematic way.

There are degeneracies that exist between the dust's location and composition which effect the temperature of dust and therefore the observed SED. However, by making assumptions that are consistent with other studies we still have a meaningful way to compare disks to each other. The SED of the disk is still a powerful way to get an initial idea of the amount of dust in the system and its physical scale.

1.2.2 Resolved studies

As mentioned in Section 1.2.1, in order to estimate the size of the disk from the SED, assumptions of grain properties must be made — generally blackbody assumptions are sufficient. However, resolving a disk directly allows for a deeper understanding of the system since the configuration and size of the disk is directly observed in resolved images. Disk sizes determined from resolved images are often found to be $\sim$2-3 times larger than those suggested by the SED with blackbody assumptions (Schneider et al., 2006; Wyatt, 2008; Matthews et al., 2010). Even resolving the disk at just one wavelength can help constrain models of the dust composition. Resolving the disk

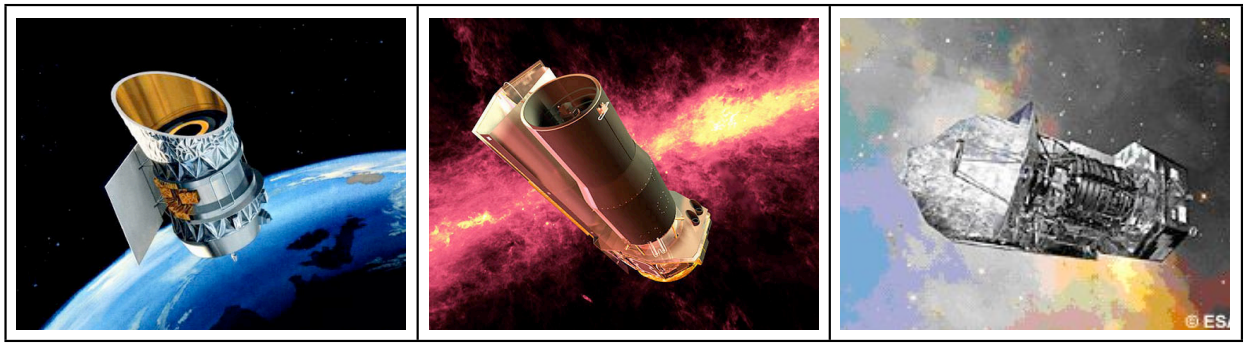

Figure 1.6 Key space-based observatories that have contributed to debris disk research: (left to right) Infrared Astronomical Satellite (*IRAS*), the Spitzer Space Telescope (*Spitzer*), and the Herschel Space Observatory (*Herschel*).

at more than one wavelength is even more advantageous as it shows whether the observed configuration of the system is wavelength dependent (e.g., Vega: Sibthorpe et al. 2010, β Leo: Churcher et al. 2011). For example, a disk may appear larger at longer wavelengths if it has two components, and the cooler one (i.e., further from the star) dominates at the longer wavelength, as is the case for η Corvi (Matthews et al., 2010).

Resolving the size of disk is beneficial for a better understanding of the dust emission's deviation from blackbody emission, but resolving the disk on smaller scales can reveal asymmetries within the disk like those discussed in Section 1.1.3. The presence of planets shaping the disk can be inferred from the detection of such asymmetries.

Resolving disks at optical wavelengths where the dust scatters the star light makes it possible to constrain dust properties (discussed in Watson et al., 2007). Determining the grain composition allows properties of the composition of the parent bodies to be inferred and therefore the formation processes that occurred in different disks, including our own, to be compared.

1.3 The Herschel Space Observatory

Debris disks are most easily observed in the far-infrared where their SED contrasts best against that of the star. However, the atmosphere is opaque at these wavelengths making space-based observatories necessary to explore this wavelength range. The field of debris disk science has been established by significant contributions from a few key observatories (see Figure 1.6). Photometric observations with *IRAS*, which

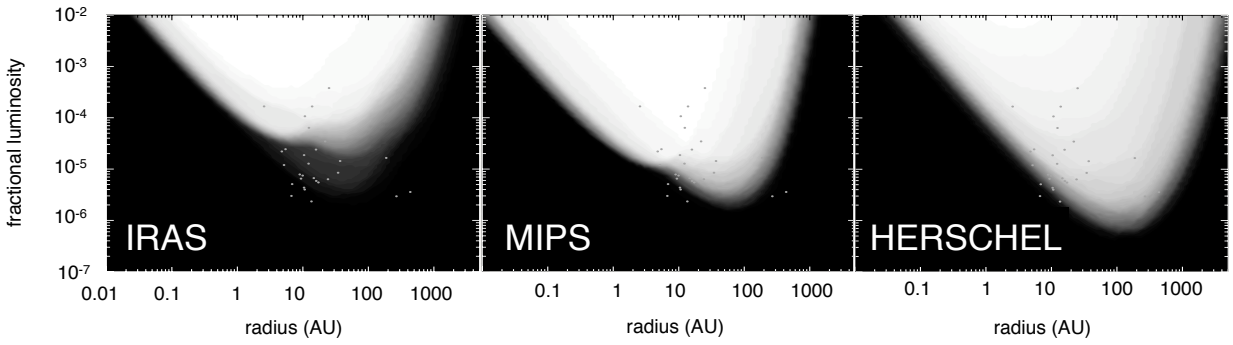

Figure 1.7 The parameter space explored for the targets in the DEBRIS sample (Section 1.5) by infrared space observatories (from left to right) *IRAS*, *Spitzer* (MIPS instrument) and *Herschel*. The stellar properties are used to infer the fractional luminosity and radius of the dust. The radius is calculated by measuring the dust temperature from the SED and assuming blackbody dust properties. (The points show the preliminary values for DEBRIS targets determined from the observations.) *Image credit: Grant Kennedy*

Table 1.2. Key contributing observatories to debris disk science

Parameter	*IRAS*				SCUBA on JCMT[a]		*Spitzer*			*Herschel*					
Mirror size [m]	0.57 m				15 m		0.85 m			3.5 m					
Far-IR/submm wavelengths [μm]	12	25	60	100	450	850	24	70	160	70	100	160	250	350	500
Resolution [$''$]	25	25	60	100	7.3	13.8	6	18	40	5	7	11	18	25	35
Launch date	25 January 1983				commissioned 1997		25 August 2003			14 May 2009					
Mission lifetime	10 months				decommissioned 2005		6 years[b]			3 years (planned)					

[a]The JCMT is a ground-based observatory.

[b]*Spitzer* continues to operate in "warm mode" taking observations in the near-infrared (at 3.6 and 4.5 μm) now that the liquid helium has been depleted.

References. — *IRAS*: Beichman et al. 1988, *Spitzer*: Rieke et al. 2004, SCUBA: Holland et al. 1999, *Herschel*: Pilbratt et al. 2010

operated at 12 μm to 100 μm, were the first to detect these dusty disks (Aumann et al., 1984). These data were unresolved and so analysis of the disks was done using the SEDs (as described in Section 1.2.1). *IRAS* only had a resolution of 25″ at 12 μm and 100″ at 100 μm (Beichman et al., 1988).[2] Not only does this make it difficult to resolve the sizes of disks, it also increases the possibility of including more than one source (especially very distant background galaxies) in the flux measurement. *Spitzer*, which observed at far-infrared wavelengths with the Multiband Imaging Photometer for *Spitzer* (MIPS, Rieke et al., 2004), was more sensitive and so probed fainter disks. Figure 1.7 shows the parameter space explored by far-infrared space observatories. The resolution of MIPS (18″ at 70 μm), however, was not enough to measure the sizes of most disks from the maps. The ESA Herschel Space Observatory (*Herschel*: Pilbratt et al. 2010) not only has the ability to detect fainter and cooler disks than *Spitzer* could (as shown in Figure 1.7) but it is also able to resolve the sizes of many disks (Matthews et al., 2010; Eiroa et al., 2010; Churcher et al., 2011; Liseau et al., 2010; Booth et al., 2012, in prep.). Table 1.2 shows the basic parameters of observatories that have had a significant impact on debris disk research.

Herschel has a 3.5 m mirror which is a significant improvement over other space-based, infrared telescopes such as *Spitzer* and *IRAS* (Table 1.2). This results in *Herschel* having better sensitivity and resolution than these observatories. *Herschel* was launched in May 2009 along with the *Planck* telescope and now orbits the second Lagrangian point of the Earth-Sun system. It is the first space telescope to bridge the wavelength gap between infrared, space-based observatories and submillimetre, ground-based observatories.[3]

Herschel has a limited lifetime determined by the amount of helium aboard to keep the instruments cool. It will operate for a minimum of three years during which it must take data for 21 Open Time Key Programmes, 21 Guaranteed Time Key Programmes, ∼500 Open Time Programmes[4] and 65 Guaranteed Time Programmes.[5] (The Key Programmes comprise 57% of the total routine time available.) To illustrate

[2] *IRAS* surveyed the entire sky and covered certain areas multiple times. Further analysis of archival *IRAS* data has produced better resolution for objects that were scanned multiple times.

[3] The Balloon-borne Large-Aperture Sub-millimeter Telescope (BLAST) also observes at submm wavelengths but is still within Earth's atmosphere.

[4] The number of accepted programmes from the 2nd announcement of opportunity has not yet been announced. There were 241 programmes accepted in the first round.

[5] Guaranteed Time is observing time reserved for the science teams that are a part of the *Herschel* project (*Herschel* Science Centre, Mission Scientists, *Herschel* Optical System Scientist, etc.). Open Time is open to worldwide scientific community.

the briefness of this time, since *Herschel*'s launch the only two opportunities for the greater astronomical community to apply for (open) time during the minimum operational lifetime have passed. During the first of these rounds, 576 proposals were received requesting a total of 20,692 hours of observing time and only a third of that time (6,577 hours) was awarded.

There are three instruments aboard *Herschel*: the Photoconductor Array Camera and Spectrometer (PACS: Poglitsch et al. 2010), the Spectral and Photometric Imaging REceiver (SPIRE: Griffin et al. 2010) and the Heterodyne Instrument for the Far Infrared (HIFI: de Graauw et al. 2010). Photometric observations using PACS and SPIRE data are used for this study and so we discuss only these instruments.

PACS simultaneously images two bands, 70 or 100 μm and 160 μm. The incoming light is split between long wavelengths and short wavelengths. The long wavelength light continues through the 160 μm "red" filter. The short wavelength light continues through either the 70 μm "blue" filter or the 100 μm "red" filter. The target can be observed at 70 μm or at 100 μm (not both), but the 160 μm observation is always taken simultaneously. SPIRE simultaneously images in three bands: 250, 350 and 500 μm.

The detectors for both the PACS and SPIRE instruments are bolometer arrays. Incident light on a bolometer increases its temperature. This results in a change of voltage across the detector since the bolometer resistance is temperature dependent.

1.4 *Herschel*'s contribution to debris disk science

Herschel operates at infrared (70, 100, 160 and 250 μm) and submm (350 and 500 μm) wavelengths, allowing it to probe much cooler disks than *Spitzer* or *IRAS* could. This opens up the parameter space of debris disks that we can study (see Figure 1.7). Furthermore, *Herschel* has better resolution than both *Spitzer* and *IRAS* at comparable wavelengths, enabling disks to be separated from nearby infrared sources such as background galaxies, and the sizes of disks to be resolved. The resolution of these different observatories (listed in Table 1.2) at ~ 70 μm exemplifies this. *IRAS* had a resolution of 60″, *Spitzer* had a resolution of 18″, and *Herschel* has a resolution of 5″.

The biggest impact that *Herschel* will have on debris disk science is through its two Key Programmes that are focused on these objects: DUNES (DUst around NEarby Stars; Eiroa et al., 2010) and DEBRIS (Disc Emission via Bias-free Reconnaissance in the Infrared/Submillimetre; Matthews et al., 2012, in prep.).

DEBRIS is a flux-limited unbiased survey of 446 stars of spectral types A through M. DUNES is a survey of nearby FGK stars designed to detect Kuiper belt analogues (cold and faint debris disks) by observing each target long enough to detect the stellar photosphere. 204 targets are shared between DEBRIS and DUNES. The data for this thesis are a part of DEBRIS and therefore DUNES will not be discussed further.

1.5 DEBRIS: An unbiased debris disk survey using the Herschel Space Observatory

We present observations of γ Dor and its debris disk that were taken with *Herschel* as a part of the DEBRIS Key Programme. The DEBRIS sample is drawn from the UNS (Unbiased Nearby Stars) sample (Phillips et al., 2010) and has been selected to be unbiased towards spectral type, binarity, metallicity and the presence of known planets, making it the first unbiased debris disk survey for cold disks since *IRAS*. All DEBRIS observations are taken to a uniform depth so DEBRIS is a flux-limited survey whose observing strategy is described in (Matthews et al., 2012, in prep.). DEBRIS' four main science goals are to determine the incidence of debris disks, characterize their evolution, resolve their size and structure and consider the Solar System (Kuiper Belt) in context.

Determine the incidence of debris disks: *Herschel* samples longer wavelengths than *Spitzer*, allowing it to probe cooler disks (see Figure 1.7). We therefore expect DEBRIS to detect the cooler, fainter debris disks which have not already been discovered by *IRAS*, *Spitzer*, or *SCUBA*. Exploring a larger parameter space results in tighter constraints on the incidence of debris disks.

Characterize debris disk evolution: The large sample size of DEBRIS targets allows us to investigate trends of debris disk properties such as radius, mass, etc, with age. This will help to identify dominant mechanisms responsible for debris disk evolution.

Resolve debris disks: As discussed in Section 1.2.2 resolving the size of debris disks has important implications on the dust location that cannot be determined from the SED alone. Understanding where the the dust is located improves our models of how and where the dust is generated within the planetesimal belt. Models of planet and planetary system formation and evolution must be

Table 1.3. Stellar information for γ Dor

Parameter	Value	Reference
UNS ID	F085	
HD number	HD 27290	
HIP number	HIP 19893	
Spectral Type	F1 V	Gray et al. (2006)
Spectral Type	F4 III	Chen et al. (2006)
RA (J2000)	04:16:01.586	van Leeuwen (2007)
Dec (J2000)	-51:29:11.933	van Leeuwen (2007)
PM-RA [mas/yr]	101.5	Høg et al. (2000)
PM-Dec [mas/yr]	184.7	Høg et al. (2000)
V magnitude	4.25	Balona et al. (1994)
Distance [pc]	20.46 $\pm$ 0.15	Phillips et al. (2010)
Age [Myr]	400	Chen et al. (2006)

able to account for the configuration and evolution of the planetesimal belt and consequently the dust. With a resolution of 6.7″ at 100 μm (300 AU at 45 pc, the distance of the furthest target), *Herschel* can probe the 10-1000 AU sizes that are typically inferred for debris disks.

Consider the Solar system in context: *Herschel*'s sensitivity allows us to probe disks that are much fainter against their host star. This allows us to study disks of similar size and brightness to the Kuiper belt, which extends from 30 to 50 AU (Jewitt & Luu, 1995) and has an inferred fractional luminosity of 10^{-7} (Backman et al., 1995).

1.6 γ Doradus

This thesis presents an analysis of the debris disk around γ Doradus (hereafter γ Dor) using observations from the Herschel Space Observatory. γ Dor is an F-type star and its basic stellar parameters are listed in Table 1.3. The brightness of γ Dor was found to vary with two periods, both slightly less than a day (Cousins & Warren, 1963). Since then evidence for a third period was found (Balona et al., 1994) and later confirmed (Balona et al., 1996). Other early F-type stars have been

found to have a similar variability as that of γ Dor and thus are referred to as γ Doradus variables (Kaye et al., 1999). The orbital motion of a companion and the presence of starspots were both found to be unlikely causes for the variability and instead non-radial gravity mode pulsations of the star are thought to be the source (Balona et al., 1994, 1996). This means that the brightness of the star is not changing because the radius is changing (as is the case for Cepheid variable stars, for example), rather certain regions of the stellar surface move outwards while others are moving inwards. Gravity mode pulsations are due to the buoyancy of the stellar material and originate from deep within the star. The fact that the γ Doradus variable stars are confined to such a narrow range of main-sequence stars (early F-types) supports that the pulsations are due to an instability in the stellar structure.

The debris disk around γ Dor was discovered with *IRAS*.[6] It has been detected with *Spitzer* but not resolved. *Herschel* is the first observatory to resolve this disk and therefore we no longer rely on the SED alone to determine the location of the dust. γ Dor is one of our well-resolved targets and therefore demonstrates how *Herschel*'s resolution, sensitivity, and wavelength range are helping to characterize individual circumstellar disks and meet DEBRIS science goals.

[6] γ Dor is not known to host any extra-solar planets but is part of the exoplanet search using Near-Infrared Coronagraphic Imager (NICI) on the Gemini-South 8.1-meter telescope (Chun et al., 2008; Liu et al., 2010).

Chapter 2

An example of an unresolved disk study: the accretion disk around the brown dwarf KPNO Tau 3

This chapter contains a study of an accretion disk around a brown dwarf and is used as an example of how to study a disk using only unresolved fluxes (see Section 1.2.1). We only know the total flux of the disk at a given wavelength, and we have no information about how that flux is arranged spatially. Brown dwarfs are not massive enough to ignite hydrogen and bridge the gap between stellar and planetary masses. These substellar objects seem to be lower mass versions of stars and so it is natural to ask how similar their formation processes are to those of low-mass stars.

KPNO Tau 3 hosts an an accretion disk (see Chapter 1 and Figure 1.1). It contains mostly gas and the brown dwarf is actively accreting material. There are a few key differences between the analysis of KPNO Tau 3's gas rich accretion disk and that of γ Dor's debris disk.

- Debris disks contain very little material compared to accretion disks. Accretion disks are very gas rich and are only 1% dust by mass. Most debris disks on the other hand do not even contain detectable amounts of gas. Moreover, debris disks typically have an order of magnitude less dust than accretion disks do. Because there is so little dust, it is optically thin everywhere as opposed to the dust in an accretion disk which is only optically thin in the submm. Therefore the dust masses of accretion disks and protoplanetary disks can only be measured using submm fluxes. Observations of the dust in the infrared are only

tracing the surface layers of the warm dust.

- Accretion disks are gas-rich and so the amount of gas in the system needs to be included in the mass measurement. Typically, it is assumed that there is 100 times more gas mass than dust mass in the disk.

- The observations of KPNO Tau 3 presented here are ground-based submillimetre observations taken with the Submillimetre Common User Bolometer Array (SCUBA) on the James Clerk Maxwell Telescope (JCMT).

2.1 Introduction

With the increase in the number of known brown dwarfs, their formation and evolution can be investigated in more detail. One recurring question regarding the origin of brown dwarfs is whether they form by the same mechanisms as low-mass stars, (e.g., turbulent fragmentation; Padoan & Nordlund, 2004), or whether they are ejected stellar embryos (Reipurth & Clarke, 2001).

The study of brown dwarf disk properties can reveal the likely origins of these objects. If the disk properties (relative to the host star) follow the same relations that are found for low-mass stars (see Jayawardhana et al., 2005), a common formation mechanism for these objects would seem likely. If brown dwarfs are ejected stellar embryos, however, their disks may appear truncated as a result of the ejection (Bate et al., 2003). Even if both mechanisms occur, observations can investigate the relative incidence of each formation scenario by determining which is most most likely for individual targets.

Detailed studies of brown dwarf disks have become more possible within the last decade. Accretion signatures and excess continuum emission due to dust reveal information on accretion disk masses, as well as dust temperatures. In particular, submillimetre emission from cold dust can imply that dust is present at large radii, contradicting the notion that the disk is truncated. It also enables the measurement of disk mass, which can then be compared to the host mass, because the submillimetre emission is optically thin.

We present submillimetre observations of three brown dwarfs, KPNO Tau 1, KPNO Tau 3 and KPNO Tau 6, in the Taurus star-forming region, to estimate their respective disk masses. We also analyze *Spitzer*/IRAC data from Luhman et al. (2010) to estimate the dust temperatures within these disks. The targets of these

observations were originally part of a larger survey to investigate brown dwarf disks using SCUBA on the JCMT. Only these three targets were observed, however, before SCUBA was decommissioned in 2005. At the time of the observations, accretion signatures had already been detected in KPNO Tau 3 and KPNO Tau 6 from Hα lines (Jayawardhana et al., 2003). Since then, further observations have been made to characterize accretion rates (Mohanty et al., 2005) and excess emission (Hartmann et al., 2005; Luhman et al., 2010) from these targets. KPNO Tau 3 and KPNO Tau 6 have Class II spectral energy distributions (SEDs), indicating the presence of a circumstellar disk, whereas KPNO Tau 1 has a Class III SED (Luhman et al., 2010), showing no evidence of circumstellar material. We investigate these sources to learn more about the systems themselves as well as to compare them to known relations between young stars and their disk properties.

2.2 Observations and Data Reduction

2.2.1 Photometry with SCUBA

Photometry observations were taken with SCUBA (Holland et al., 1999) on the JCMT in September and October 2004 at 850 μm and 450 μm. The data were reduced using the SCUBA User Reduction Facility (SURF: Jenness & Lightfoot, 1998; Jenness et al., 1998). The science observation details are summarized in Table 2.1.

The atmospheric extinction was measured by both skydip observations at 850 μm and 450 μm and by measurements from the CSO taumeter at 225 GHz at 10 minute intervals. The extinction correction was done using existing relations to extrapolate the CSO tau to extinction at the SCUBA bands using the well-established relations from the JCMT (Archibald et al., 2002) as skydips before and after the observations were not always available. Using the CSO tau values for the correction also resulted in better signal-to-noise values. It should be noted that the noise is higher in the 450 μm KPNO Tau 3 data on the first night. This is likely because these data were taken at the end of the night and therefore through more atmosphere. This affects the 450 μm data more strongly as it is more sensitive to the atmosphere.

Photometry observations of the targets were done using only the central bolometer, therefore the remaining bolometers were used to characterize the sky signal. Bolometers that proved to be noisy at any point during the night were not used (see Table 2.1). Therefore the median of the surrounding bolometers was used to remove

Table 2.1. Observing Log

Target	R.A. (J2000)	Dec (J2000)	Date observed	Integration Time (s)	# of noisy bolometers[a] 450 μm	850 μm	Flux Calibration Factor 450 μm (Jy/Volt)	850 μm (Jy/Volt)
KPNO Tau 1	04:15:14.71	+28:00:09.6	Sept 13 2004	4705	36	8	378.9 ± 10.5	243.2 ± 1.9
KPNO Tau 3	04:26:29.39	+26:24:13.8	Sept 13 2004	2326	36	8	378.9 ± 10.5	243.2 ± 1.9
			Sept 17 2004	2325	33	9	378.9 ± 10.5	243.2 ± 1.9
KPNO Tau 6	04:30:07.24	+26:08:20.8	Oct 18 2004	2299	24	14	480 ± 60	221 ± 6

[a]There are a total of 91 bolometers at 450 μm and 37 bolometers at 850 μm. The central bolometer is used for observations of the source and the remainder of bolometers (that were not noisy) are used to measure the signal of the sky.

Note. — The quality of the weather severely degraded during the night of the October observations. Therefore the fiducial FCFs for the epoch of the observations are used.

Table 2.2. RxA3 data

Line	Molecular Line	Frequency (GHz)	Noise (K)	Peak brightness (K)	Line width (MHz)
01	13-CO (2-1)	220.399	0.0114	0.50 ± 0.01	0.61 ± 0.01
02	C-18-O (2-1)	219.560	0.0111	<0.022	0.61 ± 0.01[a]

[a]Adopted from the 13-CO (2-1) line width.

the sky signal.

Uranus was used to calibrate the absolute flux scale. As is typical for SCUBA, we adopt a flux uncertainty of ∼20%. The flux calibration factors (FCFs) are given in Table 2.1. The same FCF was used for both nights in September (four nights apart) as Uranus was only observed on the second night. This was deemed reasonable as the predicted flux of Uranus changed very little between the two nights. Furthermore, the measured mean flux of KPNO Tau 3 varied little between the two nights after FCF correction. Although Uranus was observed multiple times during the night of the October observations there was a sharp increase in the atmospheric extinction making it difficult to measure FCFs. Thus the fiducial FCFs for the epoch of the observations are used instead.

The means of the individual integrations were found to determine whether or not there was a significant measurement of flux. After clipping data points $> 3\ \sigma$ from the mean, we took the mean over all the remaining photometric measurements.

2.2.2 Spectroscopy with Receiver A3

Follow-up spectroscopy was done using Director's Discretionary Time on the JCMT on 25 January 2011 at 220 GHz. The 13-CO (2-1) and C-18-O (2-1) lines were observed. The science observation details are summarized in Table 2.2. Data were reduced using the Sub-Millimetre User Reduction Facility (SMURF: Jenness et al., 2008) and the VO enabled Spectral Analysis Tool (SPLAT: Draper, P. W. et al., 2005).

Baselines were fit to the regions of the spectra that did not contain the spectral line of interest or the noisy ends of the spectra. The noise in each spectrum is listed

with the target molecular lines in Table 2.2.

2.3 Results

2.3.1 Detections

Photometry

The criterion for a detection is the measurement of a non-zero mean that is at least 3 σ where σ is the statistical error after clipping. Table 2.3 summarizes the submillimetre flux measurements for KPNO Tau 1, KPNO Tau 3 and KPNO Tau 6. With this criterion only KPNO Tau 3 had a significant flux detection at 450 and 850 μm. KPNO Tau 3 was observed on two separate nights, each of which independently had a 2 σ detection at 850 μm. Combining the 850 μm observations from the two nights yields a 3 σ detection in this band. A 3 σ detection at 450 μm is present from the data on the second night. Including the 450 μm data from the first night, however, adds noise due to the high extinction of those data (see Section 2.2). Therefore, we use only the 450 μm data from the 17 September 2004 for subsequent analysis. For the other two targets, KPNO Tau 1 and KPNO Tau 6, the 2 σ upper limits on the flux are quoted in Table 2.3.

Spectral Line Observing

The spectra are shown in Figure 2.1. A 13-CO spectral line is observed and fit with a gaussian profile to measure the peak brightness, 0.50 $\pm$ 0.01 K, and FWHM, $\Delta\nu$ = 0.61 $\pm$ 0.01 MHz, of the line. There is no line observed in the C-18-O spectrum so the 2 σ upper limit of 0.022 K on the peak brightness that could be observed and the 13-CO line width are adopted for the analysis.

2.3.2 Modelling of photospheric emission

To analyze the emission originating from a disk, it is necessary to characterize the expected photospheric emission of the host brown dwarf. The predicted photospheric emission can then be subtracted from the observed emission to determine the excess emission due to dust.

NextGen models (Allard et al., 1997), which include brown dwarfs with effective temperatures as low as $\sim$1500 K, are fit to HST (Kraus et al., 2006) and 2MASS (Cutri

Table 2.3. Flux measurements and disk properties

Target	F_{450} (mJy) (1)	F_{850} (mJy) (2)	$M_{disk,450}$ (10^{-4}M$_\odot$) (3)	$M_{disk,850}$ (10^{-4}M$_\odot$) (4)	M$_{disk}$ (10^{-4} M$_\odot$) (5)	Single temperature (K) (6)	Single temperature Resulting χ^2 (7)	Two-temperature (K) (8)	Two-temperature Resulting χ^2 (9)
KPNO Tau 1	<23.2	<3.4	<3.0	<2.0	<2.0	–	–	–	–
KPNO Tau 3	47.7 ± 15.7	5.9 ± 1.9	6.1 ± 2.3	3.5 ± 1.3	4.5	437	87.0	242 & 773	0.5
KPNO Tau 6	<20	<7.2	<2.5	<4.2	<3.0	575	24.0	268 & 794	0.1

Column key:
(1) 450 μm fluxes measured in Section 2.3.1. 2 σ upper limits are given for KPNO Tau 1 and KPNO Tau 6;
(2) 850 μm fluxes measured in Section 2.3.1. 2 σ upper limits are given for KPNO Tau 1 and KPNO Tau 6;
(3) Disk mass determined from 450 μm flux in column (4) using Equation 2.1;
(4) Disk mass determined from 850 μm flux in column (4) using Equation 2.1;
(5) Disk mass determined from the χ^2 minimization fit to the 450 and 850 μm data described in Section 2.3.4;
(6) Temperature of a single temperature model of mid-infrared excesses described in Section 2.3.4;
(7) The resulting χ^2 for the single temperature model;
(8) Temperatures of a two temperature model of mid-infrared excesses described in Section 2.3.4;
(9) The resulting χ^2 for the two temperature model.

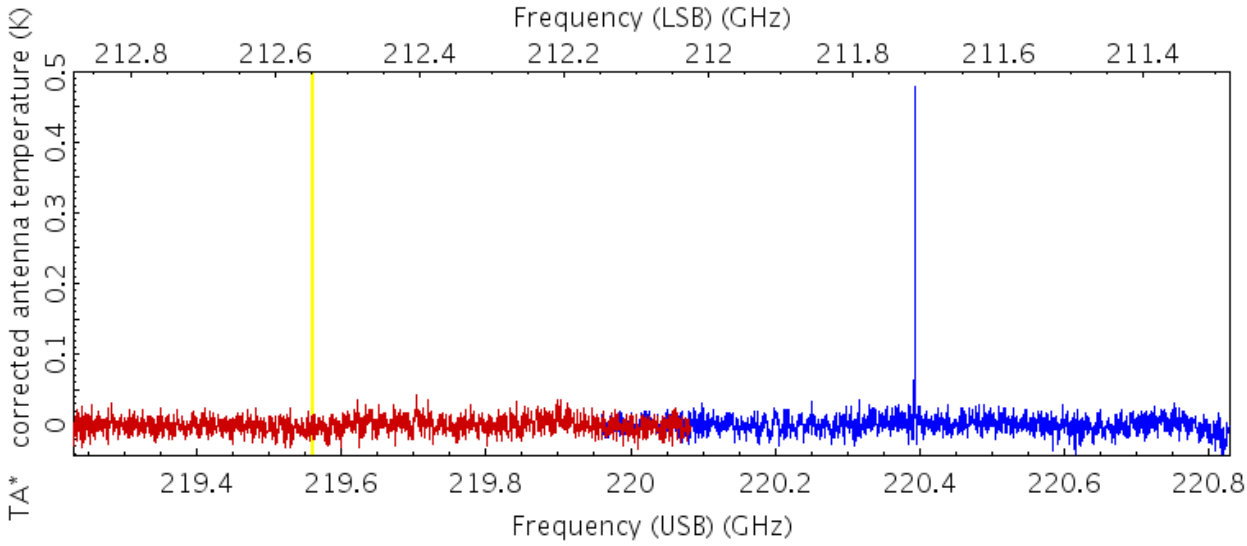

Figure 2.1 The spectra containing C-18-O(2-1) *(red)* and 13-CO(2-1) *(blue)* lines are shown. No spectral line is detected for C-18-O at 219.56 GHz *(yellow vertical line)*.

Table 2.4. Brown dwarf properties

Target	M_* ($M_\odot$) (1)	$T_{\rm eff}$ (K) (2)	$\log(g)$ (3)
KPNO Tau 1	0.02 ± 0.01	2600	-0.5
KPNO Tau 3	0.077 ± 0.009	3000	0.0
KPNO Tau 6	0.021 ± 0.007	2600	-0.5

Column key:
(1) Brown dwarf masses are from Kraus & Hillenbrand (2009);
(2) $T_{\rm eff}$ are from Briceño et al. (2002);
(3) $\log(g)$ values are determined from the photospheric modelling in Secion 2.3.2.

et al. et al., 2003) photometry to determine the predicted photospheric flux. These models are produced with a variety of effective temperatures ($T_{\rm eff}$), gravities ($\log(g)$), abundances, and alpha enhancements. We assume solar metallicity without alpha enhancement for this analysis. We adopt effective temperatures, listed in Table 2.4, from studies based on spectroscopic data (Briceño et al., 2002) as this is a more precise method than SED modelling of photometric data. This allows us to fit for $\log(g)$.

To determine the optimal photospheric model, χ^2 fits were performed on models with various $\log(g)$ values. After normalizing the model to the observed K_s flux, the fits were done by comparing the 2MASS and HST observations to the local average of the model at the effective observed wavelengths. The fluxes at these wavelengths are assumed to follow the photosphere (i.e., we do not expect any excesses in these bands). Mid-infrared and submillimetre excess emission for each object was determined by subtracting the respective model photospheric flux from the observed *Spitzer* (Luhman et al., 2010) and SCUBA fluxes. Table 2.3 shows the parameters of the best fit models. Figures 2.2, 2.3 and 2.4 show the SEDs for KPNO Tau 1, KPNO Tau 3 , and KPNO Tau 6, respectively.

2.3.3 Determining Disk Masses

The disk mass is determined from the 450 μm and 850 μm fluxes. This emission is assumed to originate in the optically thin cold dust that dominates the disk mass.

The mass of the disk, M_{disk}, can be determined from the flux density of the dust, F_{dust}, by

$$M_{disk} = \frac{F_{dust} D^2}{\kappa_\nu B_\nu(T)} \tag{2.1}$$

where D is the distance to the source (140 ± 10 pc for Taurus, Kenyon et al., 1994), κ_ν is the opacity of the dust grains, and $B_\nu(T)$ is the Planck function for temperature, T. A temperature of 20 K is assumed and the opacity is assumed to be $\kappa_\nu = 0.1(\nu/1000\ \mathrm{GHz})\ \mathrm{cm^2 g^{-1}}$, following previous studies of the Taurus region (Andrews & Williams, 2005; Beckwith et al., 1990). (This opacity relation includes the assumed dust-to-gas ratio of 1:100.) Although there may be systematic uncertainties in the assumptions on κ_ν and T, these assumptions are consistent with other studies of the Taurus star-forming region and therefore are valid to compare our results to those found for classical T-Tauri stars in this region.

The disk masses for KPNO Tau 3 (and upper limits for KPNO Tau 1 and KPNO Tau 6) are determined using the 450 and 850 μm fluxes independently and shown to agree within the uncertainties and are listed in Table 2.3. The disk mass for KPNO Tau 3 is also determined using a χ^2 fit to the SED, the parameters of which are summarized in Table 2.3. The relative disk to host mass for KPNO Tau 3 is then $\sim$0.6%. This relative disk mass is within the range of $\lesssim$1% and 5% that has been found for other brown dwarfs and agrees with the values for low mass T Tauri stars (Scholz et al., 2006).

2.3.4 Determining Disk Temperatures

The presence of warmer dust in the disks of KPNO Tau 3 and KPNO Tau 6 is indicated by the mid-infrared excesses in their SEDs. Luhman et al. (2010) used IRAC observations to determine the SED class of these targets, and we extend their analysis to determine disk temperatures by fitting blackbodies to the excess emission. The temperatures of the dust in these disks were determined by analyzing solely the IRAC data from Luhman et al. (2010). The flux of the 20 K dust, used to determine the disk mass in Section 2.3.3, is negligible at the mid-infrared wavelengths and therefore not included. Disk temperatures are not derived for KPNO Tau 1 as this object has no detectable mid-infrared excesses.

Both single-component (i.e., single temperature) and two-component blackbody χ^2 fits were performed on the *Spitzer* data to demonstrate that the mid-infrared emission is not due to just one dust population. A range of temperatures is expected in the disk, however with our limited number of data points, we can only fit for two components. The fitted parameters are shown in Table 2.3 with their χ^2 values to show how the two-component model is more suitable. The highest temperature belongs to the dust grains that are closest to the star and can therefore be used to constrain the disk's inner radius. The two-component blackbody fits are compared to the observations in Figures 2.2, 2.3 and 2.4.

2.3.5 13-CO and C-18-O toward KPNO Tau 3

The SED of KPNO Tau 3 suggests that it is a Class II object (Luhman et al., 2010), a young substellar object whose circumsubstellar material is located in a disk. However, it is possible that some Class II objects, classified by their SEDs, are actually Class I objects with a remnant envelope (Evans et al., 2009). Such an SED could resemble

that of a Class II because of the viewing geometry. We took observations of C-18-O (2-1) to place constraints on the amount of mass that could be in a dense remnant envelope. (C-18-O is an effective tracer of dense material.)

At ∼230 GHz, the JCMT has a beam efficiency of 0.60. We use this to determine the brightness temperature, T_B from the antenna temperature, T_A^*. The optical depth, $\Delta\tau$ is calculated using

$$T_B = T_o\ [f(T_{ex}) - f(T_{bg})]\ [1 - \exp(-\Delta\tau_o)] \tag{2.2}$$

where $T_o = h\nu_o/k$ and $f(T) = [\exp(\mathrm{T_o/T}) - 1]^{-1}$. ν_o is the frequency at line centre listed in Table 2.2, h is the Planck constant and k is the Boltzmann constant. The excitation temperature, T_{ex}, is equal to the kinetic temperature of the dust, 20 K, (discussed in Section 2.3.3) assuming that the cloud is in local thermodynamic equilibrium. The background temperature, T_{bg}, is that of the cosmic microwave background, 2.73 K. Both isotopes are found to be optically thin ($\Delta\tau_o << 1$) with $\Delta\tau_o$ of 0.050 and <0.0021 for 13-CO (2-1) and C-18-O (2-1), respectively.

The column density, N, is given by

$$N = \frac{8\pi\nu_o^2\Delta\nu Q\Delta\tau}{c^2 A_{21}}(\frac{g_2}{g_1})[1 - e^{-T_o/T_{ex}}]^{-1} \tag{2.3}$$

where the partition function, Q, is $\sim 2T_{ex}/T_o$. g_2 and g_1 are the statistical weights of the J=2 and J=1 rotational levels, respectively. A_{21} is the Einstein coefficient for the 2-1 transition and has values of $10^{-6.22}$ (Klapper et al., 2000) and $10^{-6.22}$ (Klapper et al., 2001) for 13-CO and C-18-O, respectively.[1] $\Delta\nu$ is measured for the 13-CO line and assumed to be the same for the C-18-O line.

The measured column density of 13-CO is $\sim 10^{14.58}$ cm^{-2} and that for C-18-O is $< 10^{13.21}$ cm^{-2}. Given the column density of 13-CO, were there an envelope around KPNO Tau 3, one would expect to N(13-CO)/N(C-18-O) in the range of 10 - 16, as is found for dark clouds (Zhu et al., 2007; Kim et al., 2006). However we find N(13-CO)/N(C-18-O) > 20, implying that we are not observing the dense material in a circumsubstellar envelope and that the dust emission arises entirely from a circumsubstellar disk.

[1]Line information collected from the Splatalogue database for astronomical spectroscopy.

2.4 Discussion

Our submillimetre data show that KPNO Tau 3 has a significant cold component of dust suggesting a disk mass of $\sim 4.5 \times 10^{-4}$ $M_{\odot}$. We have placed upper limits on the disk masses for KPNO Tau 1 and KPNO Tau 6 that are a factor of $\sim$2 more stringent than those determined from observations at 1.33 mm (Scholz et al., 2006).

We assume that all the dust detected towards KPNO Tau 3 lies in a circumsubstellar disk and not in a remnant envelope. This is because young objects with an envelope can have similar SEDs to young objects with disks if the envelope's opening is directed towards us. We investigated the possibility of KPNO Tau 3 having a remnant envelope by taking observations of 13-CO (2-1) and C-18-0 (2-1). Both species are measured to be optically thin and the relative abundance of 13-CO to C-18-O, >20, is higher than what is found towards objects with envelopes, usually in the range of 10 - 16 (Zhu et al., 2007; Kim et al., 2006). Furthermore, KPNO Tau 3 is in a region of relatively low extinction, $A_v \sim 1.6$ (determined from Dobashi 2011 dust maps), implying it is less likely to be in an envelope since they are found in denser regions.

The composite SEDs show that the disks around KPNO Tau 3 and KPNO Tau 6 contain dust at various temperatures. This is expected if one is observing emission originating from different locations in the disk, as is observed with T Tauri stars. The presence of cold, 20 K dust can imply that dust is present at large radii. This favours a formation mechanism for brown dwarfs that is similar to that of stars, since an ejected stellar embryo scenario would have a truncated disk. Furthermore, the amount of cold dust that is in the KPNO Tau 3 disk is suggestive of the system being a lower-mass analogue of a T Tauri star. This is shown by considering the relative disk mass for KPNO Tau 3 of 0.6%. This values lies within the range that is found for low-mass T Tauri stars, $\lesssim$1% to 5%. It is unfortunate that SCUBA was decommissioned before this survey could be completed. A similar study should be investigated with SCUBA-2, which is now undergoing science verification and expected to start open observing in February 2012, to look for cold dust indicative of large disks and to measure relative dust masses for accretion disks around brown dwarfs.

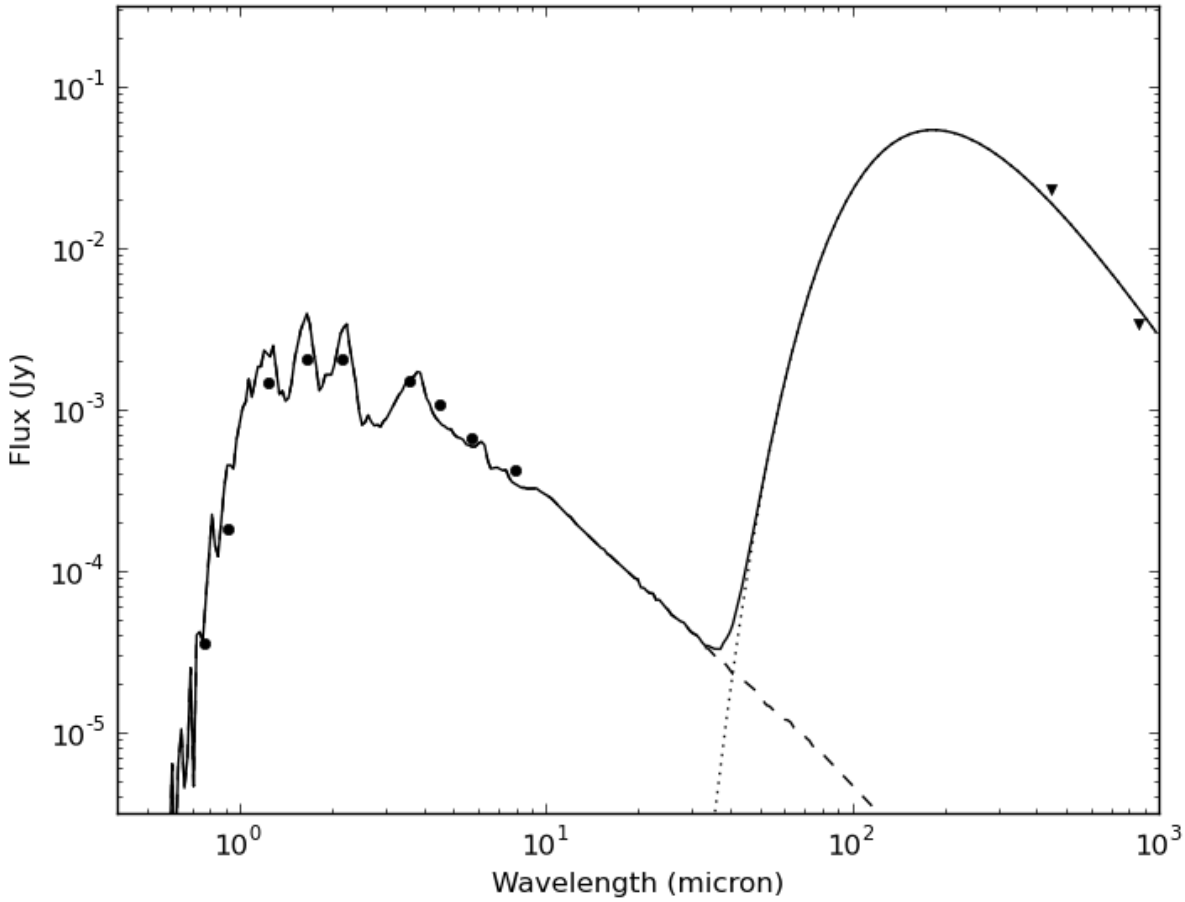

Figure 2.2 The SED for KPNO Tau 1. The *dashed line* shows the expected photospheric emission of KPNO Tau 1 using NextGen models that adopt the spectral type determined from observations. There is no excess observed in the mid-infrared with *Spitzer*. The upper limits *(triangles)* determined with SCUBA place an upper limit on any possible disk mass of 2.5×10^{-4} $M_{\odot}$.

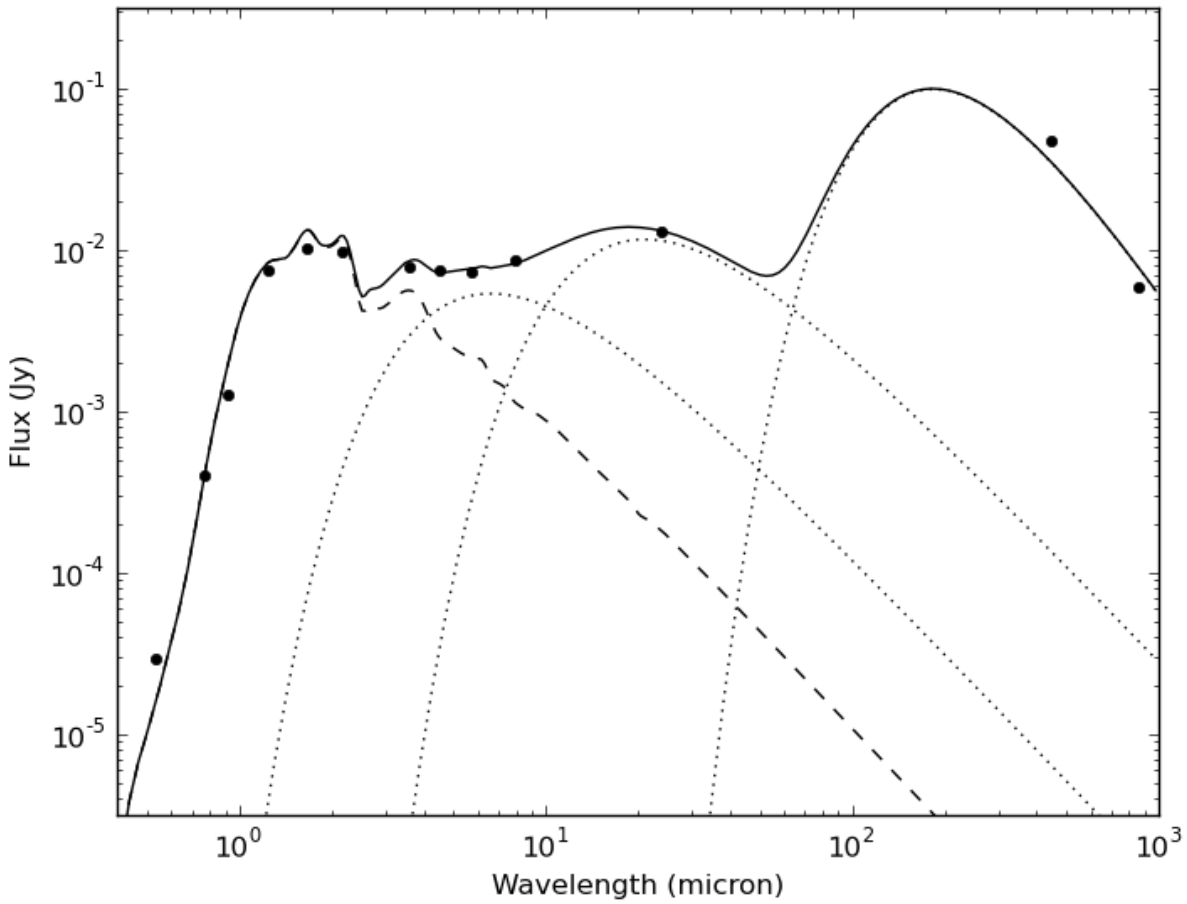

Figure 2.3 The SED for KPNO Tau 3. The *dashed line* shows the expected photospheric emission of KPNO Tau 3 using NextGen models that adopt the spectral type determined from observations. The *dotted lines* show blackbody fits at 770 K, 240 K and 20 K *(left to right)*. The two temperature fit to the mid-infrared emission determines temperatures of 770 K and 240 K. The blackbody fit to the submillimetre emission assumes a temperature of 20 K and is modified to account for varying opacity across submillimetre wavelengths, estimating a disk mass of 4.5×10^{-4} $M_{\odot}$.

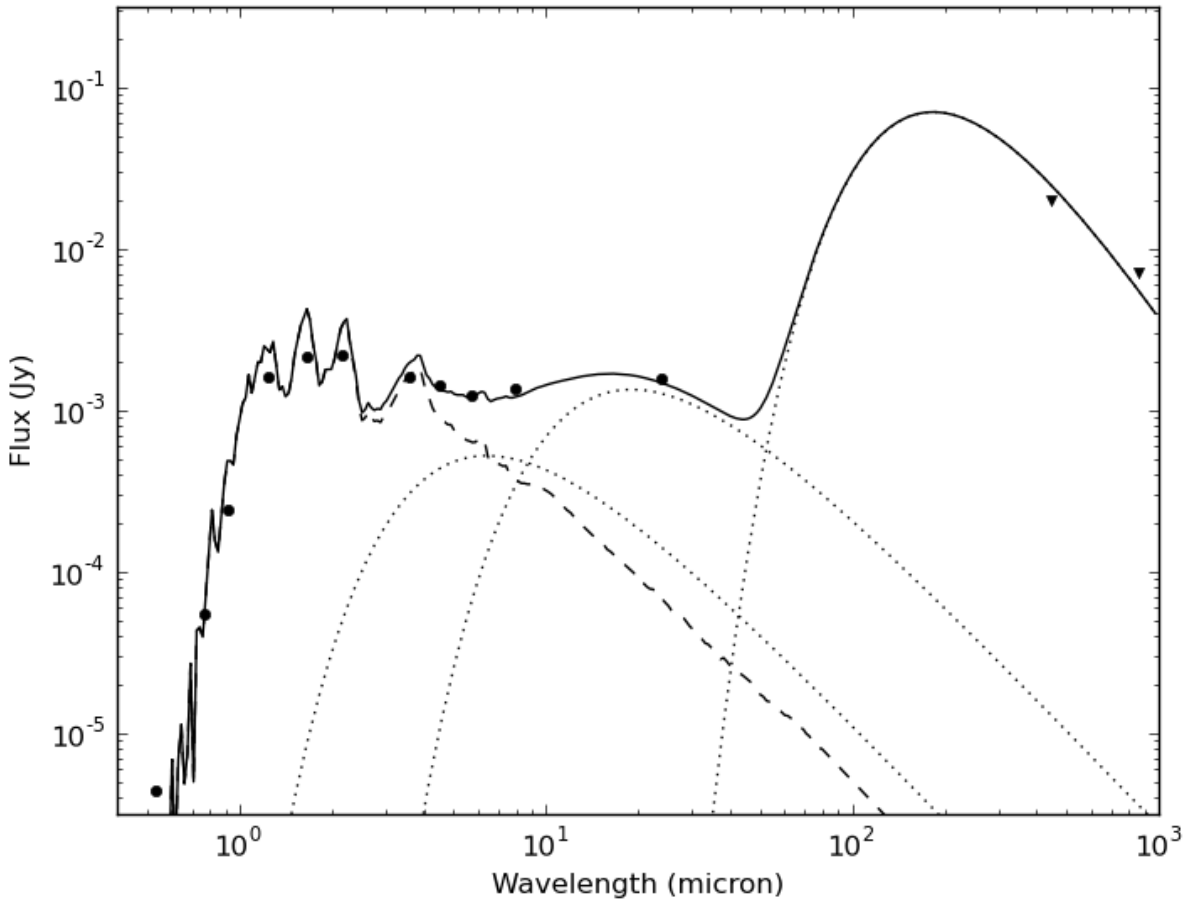

Figure 2.4 The SED for KPNO Tau 6. Line styles are as in previous figures. The temperature fits for KPNO Tau 6 are 790 K and 270 K *(left to right)*. A 20 K modified blackbody fit to the SCUBA upper limits *(triangles)* determines an upper limit on the disk mass of 2.5×10^{-4} $M_{\odot}$.

Chapter 3

Observations of γ Dor

3.1 *Herschel* data

The PACS (70, 100 and 160 μm) and SPIRE (250, 350 and 500 μm) observations were taken in the scan-map and small-map modes, respectively. Both of these observing modes involve the telescope scanning along two directions. The PACS and SPIRE scan directions are 40° and 85° apart, respectively. The coverage maps in Figure 3.1 show the relative amount of time that the telescope observes each point in the sky. The target is at the centre of these maps. Table 3.1 lists the observing parameters. The PACS observations are taken with a scanning rate of 20″/s. It observes simultaneously either at 100 and 160 μm or at 70 and 160 μm. DEBRIS observes all its targets at 100 and 160 μm but followed up γ Dor and fifteen other targets at 70 μm. The 70 μm observation of γ Dor was requested to help constrain the modelling and separate out the background source from its flux measurement. As a result, γ Dor was observed at 160 μm twice, and the map at this wavelength is composed of data from both observations.

The PACS data were reduced using HIPE (*Herschel* Interactive Processing Environment: Ott 2010) version 7.0 Build 93. All data sets in the DEBRIS survey are reduced in the same way (described in Sibthorpe et al., 2012, in prep.). The reduction method includes "turn-around" data that were taken while the telescope was reversing the scan direction and therefore not scanning at a constant speed. This increases the coverage everywhere on the map and reduces the noise at its centre (where the target is located) by ∼25% (Matthews et al., 2012, in prep.). Figure 3.1 shows that the centre of the PACS maps are no longer the region with the highest coverage. The

Table 3.1. *Herschel* data

Instrument	Band (μm)	Time on target (seconds)	Observation date(s)	Beam size[a] (arcsec)	Measured noise in the maps PSF[b] (mJy/beam)	Aperture[c] (mJy/beam)	DEBRIS[d] (mJy/beam)	Flux of γ Doradus system PSF (mJy)	Aperture (mJy)	2D Gaussian[e] (mJy)
PACS	70	1129	29 Apr 2011	5.46 x 5.76 (5.61)	1.2	0.8	1.3 [h]	116[i]	170.6 ± 1.7	137.5 ± 1.4
PACS	100	1129	31 Mar 2010	6.69 x 6.89 (6.79)	1.3	0.8	1.0 ± 0.2	98.3[i]	148.4 ± 1.5	125.7 ± 1.7
PACS	160	2258[f]	31 Mar 2010 29 Apr 2011	10.65 x 12.13 (11.36)	3.4	1.8	2.1 ± 0.2	89.9[i]	134.3 ± 1.2	122.0 ± 1.9
SPIRE	250	901	21 Sep 2010	18.7 x 17.5 (18.2)	4.9	4.1	6.33 ± 1.30	58.0 ± 1.9	57.4 ± 2.6	66.2 ± 5.3
SPIRE	350	901	21 Sep 2010	25.6 x 24.2 (24.9)	7.3	–[g]	6.18 ± 1.00	32.1 ± 2.0	24.9 ± 3.2	22.9 ± 4.6
SPIRE	500	901	21 Sep 2010	38.2 x 34.6 (36.3)	5.3	4.1	6.39 ± 0.89	<16.7 ± 2.3[j]	–	–

[a]The effective beam size (geometric mean) is listed in parentheses.

[b]The PSF noise is determined by fitting PSFs to random locations within a region that has similar coverage to that at the map centre.

[c]The aperture nose is determined by measuring the flux within an aperture (with a radius that is the size of the effective beam radius) at random locations within a region that has similar coverage to that at the map centre.

[d]The median value of the noise measured in all DEBRIS maps by measuring the flux within randomly placed apertures.

[e]Taken to be the integral of 2D Gaussian fits to γ Dor's position. (It therefore estimates the total flux of the star and disk system).

[f]The target was observed at 160 μm simultaneously with both the 70 and 100 μm observations and so the data from each of these observations are combined.

[g]The distribution of measured fluxes in the map does not follow a well-defined single Gaussian.

[h]PACS 70 data was only taken for 16 DEBRIS targets.

[i]γ Dor is resolved at 70, 100 and 160 μm causing the fitted PSF to miss the extended structure and underestimate the total flux.

[j]This flux includes the nearby background source.

References. — Beam sizes from PACS Observer's Manual and SPIRE Observer's Manual. Survey values from Matthews et al. (2012, in prep.).

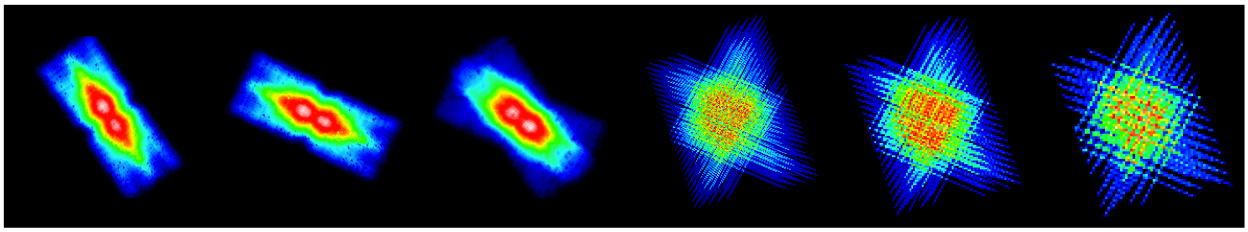

Figure 3.1 Coverage maps at *(left to right)* 70, 100, 160, 250, 350 and 500 μm. These show the relative amount of time each point on the sky is observed. The observing modes are designed to have the highest coverage *(white region)*, and therefore the lowest noise, at the centres of the maps. Including the "turn-around" data in PACS maps (see text) increases the coverage everywhere, however, the centre of the map no longer has the highest coverage. Note that the PACS maps are 3.5′ by 8′ and the SPIRE maps are 12′ by 14.5′.

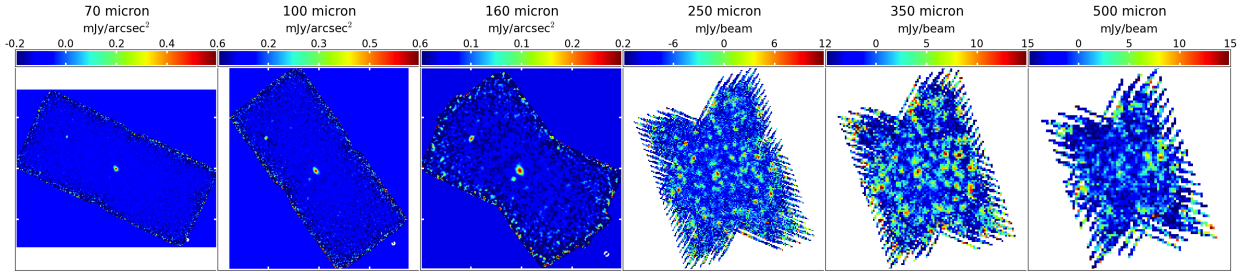

Figure 3.2 The full-sized maps at *(left to right)* 70, 100, 160, 250, 350 and 500 μm. These show how the maps are populated by background sources, especially at SPIRE wavelengths. Note that the PACS maps are 3.5′ by 8′ and the SPIRE maps are 12′ by 14.5′.

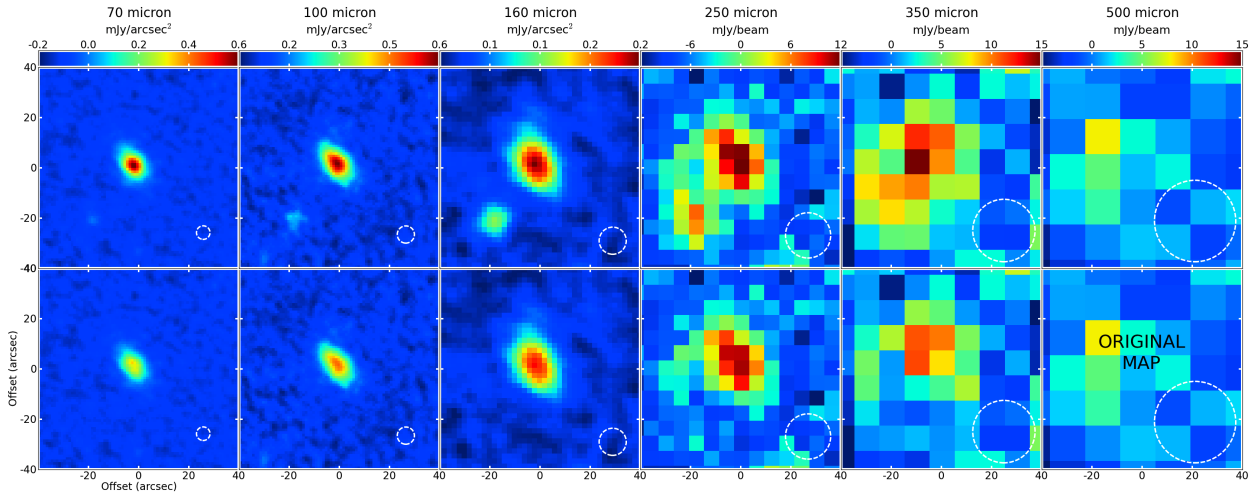

Figure 3.3 The *top panels* show the observations at 70, 100, 160, 250, 350 and 500 μm *(left to right)*. The *bottom panels* show the maps at the same wavelengths where the stellar photospheric model and the fitted PSF to the nearby background source (to the southeast of γ Dor) have been subtracted for cosmetic improvement to the images. No sources have been subtracted at 500 μm because the contributions of each source cannot be disentangled. Beam sizes are shown in the bottom right corners.

Table 3.2. Archival *Spitzer* IRS data

Band (μm)	AOR 24368640 Fractional excess[a]	Dispersion	Strength of excess[b]	AOR 27577600 Fractional excess[a]	Dispersion	Strength of excess[b]
6-7	–	–	–	0.0115	0.0037	1.1
8-10	–	–	–	0.0068	0.0042	0.63
18-20	0.022	0.008	1.7	0.0146	0.031	0.44
23-25	0.038	0.03	1.2	0.0038	0.020	0.17
30-34	0.18	0.035	5.1	0.161	0.064	2.5

[a]Excess flux divided by the expected flux.

[b]The fractional excess divided by the quadratic sum of the dispersion in γ Dor's spectrum and the dispersion in the total sample of spectra of DEBRIS targets. A strength > 3 indicates a strong excess and a strength between 2 and 3 indicates a marginal excess.

Note. — AOR 24368640 and AOR 27577600 spectra span 14-35 and 5.5-35 μm, respectively.

PACS data have been high-pass filtered to remove 1/f noise. The filtering at 70, 100 and 160 μm corresponds to angular filter scales on the sky of 66, 66 and 100″. The SPIRE data were also reduced using the standard *Herschel* pipeline script in HIPE. Figure 3.2 shows the full-sized maps and the region around the target is enlarged in Figure 3.3. The properties of the beams and maps using these instruments are listed in Table 3.1.

3.2 *Spitzer* data

We have included archival *Spitzer* data (AORs[1] 24368640 and 27577600) taken using the InfraRed Spectrograph (IRS). This is done for stars in DEBRIS for which archival IRS data are available (about 150 targets in total). (Only AORs taken in stare-mode were included, therefore AOR 3555584 from Chen et al. 2006, taken in map-mode, is excluded.) The data reduction procedure follows that described in Lawler et al. (2009) except for the use of a "superflat" (an average of the spectra of stars without

[1]An Astronomical Observation Request (AOR) is an identification key assigned to each observation of a target.

excesses used to identify and remove instrumental features in the spectra). Because the spectra were gathered from the *Spitzer* data archive and are not all part of a uniform survey, attempts to create and apply superflats for different groups of stars (defined by the time of the observations, or by stellar spectral type) did not result in decreased noise for the spectra, and so the superflat step was abandoned. This should not significantly decrease the quality of the spectra as the *Spitzer* data reduction pipeline has also improved since Lawler et al. (2009), decreasing the need for a superflat step.

The dispersion in the total sample of IRS spectra of DEBRIS targets (about 150) and the dispersion of γ Dor's spectrum are both included in the uncertainty listed in Table 3.2. During the reduction of each spectrum of γ Dor, the spectrum is pinned to the photosphere at the shortest wavelengths and therefore assumes there is no excess shortward of $\sim$14.5 μm. This is reasonable for γ Dor, as there is no known excess due to hot dust. (The validity of this assumption can be examined once the results on the census for warm dust around known debris disks using 3.6 and 4.5 μm IRAC observations led by K. Su are known.) Table 3.2 summarizes the data by listing the fractional excess[2] within different sections of each spectrum. It also lists the dispersion of the fractional excess within each section and relates it to the dispersion in the overall sample of IRS spectra for DEBRIS targets. A significant fractional excess of 0.18 is detected in the 30-34 μm section for AOR 24368640. Chen et al. (2006) find a fractional excess of 0.147 in the 30-34 μm band (they observe 194 $\pm$ 2 mJy where 170 mJy is predicted). However, our errors should be inflated when comparing to other surveys. Furthermore, Chen et al. (2006) was one of the first IRS papers and so they used slightly different photospheric models.

We also coadd the two AORs, weighted by their errors, to compare the IRS data to photometry observations. We expect the values to be within 10% of each other. To compare the spectrum to the MIPS 24 μm flux, we calculate the average of the data within the MIPS 24 μm passband weighted by the responsivity of the filter. We do not include the IRS data in the SED modelling (in Section 4.4) to avoid issues of the disk not being resolved with IRS or some of the flux falling outside the slit, but do superimpose them to our results for comparison (Figure 4.1). They are within 10% as expected.

[2]The ratio of the excess flux to the expected stellar photospheric flux.

Chapter 4

Results & Analysis

4.1 Modelling the stellar photosphere

Accurate models of the stellar photosphere are crucial for debris disk studies, as the analysis is based on emission that is observed in excess of expected photospheric emission. This is especially important for unresolved sources where this is the only evidence that a disk is present. The stellar photosphere is modelled using a χ^2 minimization method to fit stellar models from the Gaia grid (Brott & Hauschildt, 2005). The modelling of the stellar photosphere is done consistently for all DEBRIS targets and the procedure is described in detail in Kennedy et al. (2012, in prep.). The $\sim$1% optical variability of γ Dor does not affect the photospheric modelling since the photometry is not sensitive to these variations. Furthermore, variations on this scale will not alter our conclusions on the far-IR emission where the disk is much brighter than γ Dor.

Archival data from many instruments are included to model the stellar photosphere. The values for the fitted parameters of the photospheric model are listed in Table 4.1 along with stellar parameters measured by other studies. Given the uncertainties in deriving $\log(g)$ and [M/H] from SED modelling, the results are in good agreement (within 0.1 dex and 0.3 dex, respectively) of Gray et al. (2006). The difference from Gray et al. (2006) will not significantly alter our results given the high contrast of the disk's emission to the stellar emission at *Herschel* wavelengths. The predicted photospheric fluxes from the stellar fit are listed in Table 4.2 along with the observed fluxes.

Table 4.1. Fitted stellar parameters

Parameter	DEBRIS	Gray06	Chen06	DeCat06
$T_{\rm eff}$ [K]	7204 ± 28	7060	7290	...
$\log(g)$ [cm/s^2]	3.49 ± 0.1	3.97	3.97	...
[M/H]	-0.41 ± 0.17	-0.13	...	...
R_* [R$_\odot$]	1.67 ± 0.22	...	...	...
M_* [M$_\odot$]	∼1.6	...	...	...
L_* [L$_\odot$] [a]	6.7 ± 0.1	...	...	...
χ^2_{dof}	0.441	...	...	...
$v \sin i$ [km/s]	...	...	65	55 ± 2
Age [Gyr][b]	...	...	0.40	...

[a] L_* is found from the fitted R_* and $T_{\rm eff}$.

[b] The age is determined by fitting $\log(g)$ and $T_{\rm eff}$ to Schaller et al. (1992) isochrones. The uncertainty is estimated to be a factor of 2.

References. — DEBRIS, Kennedy et al. 2012, in prep.; Gray06, Gray et al. 2006; Chen06, Chen et al. 2006; DeCat06, De Cat et al. 2006

4.2 Flux measurement

The method used to measure the flux depends on whether or not γ Dor's disk is resolved at the wavelength in question. The target is first treated as a point source and fit with a point-spread function (PSF). If the target is indeed an extended source this will be evident in the residuals of the PSF fit. Therefore PSF fitting is done at all wavelengths because this will either provide a flux measurement or an indication of whether the target is extended or resolved. The flux of resolved sources is measured with aperture photometry and verified by the integral of 2D Gaussian fits to the source to ensure that features like flux contributions from background sources are not included. Aperture photometry is used to determine fluxes at 70, 100 and 160 μm. PSF fitting is used to determine fluxes at 250, 350 and 500 μm. The flux at 500 μm includes flux from both γ Dor and the background source and so it is quoted as an upper limit for the disk flux alone. The measured fluxes are displayed in the SED in Figure 4.1 and listed in Table 4.2 along with the preferred method used to measure them.

The uncertainty in aperture photometry is taken from the error in the sum of the flux within the defined region. The uncertainty in the flux measurement from fitted PSFs is determined from the uncertainty in the fit itself. In addition to these, each instrument carries its own uncertainties which need to be included. The PACS calibration accuracies of 5%, 5% and 10% at 70, 100 and 160 μm, respectively, and SPIRE pixel size correction factors and absolute flux calibration accuracy of 7% are added in quadrature.

The maps are calibrated assuming the target has a flat spectrum, however γ Dor's SED falls off in the submillimetre with a spectral index of $\sim$2. Colour corrections of 0.9692 and 0.9744[1] have been applied to 250 and 350 μm fluxes, respectively, to account for the declining spectrum through SPIRE filters. The 250 μm colour correction includes an extended source correction since γ Dor's disk is resolved at this wavelength along its long axis. (PACS colour corrections were unnecessary for the observed fluxes.)

Table 4.2. Observed fluxes and predicted photospheric fluxes

Wavelength (μm)	Observed flux[a] (Jy)	Instrument or Satellite	Method	Model photosphere (Jy)	Excess (Jy)	Reference
0.4	59.8 ± 0.8	Hipparcos	-	59.7 ± 1.1	...	Høg et al. (2000)
0.5	74.4 ± 0.8	Hipparcos	-	74.8 ± 1.4	...	Høg et al. (2000)
0.6	71.5 ± 1.4	Hipparcos	-	71.7 ± 1.3	...	Perryman & ESA (1997)
0.5	76.5 ± 1.5	Hipparcos	-	75.7 ± 1.4	...	Mermilliod (2006)
1.2	53.7 ± 12.0	2MASS	-	55.2 ± 1.0	...	Cutri et al. et al. (2003)
9.0	1.9080 ± 0.0350	AKARI	-	1.9240 ± 0.0350	...	Ishihara et al. (2010)
12.0	1.2020 ± 0.0510	IRAS	-	1.1790 ± 0.0220	...	Moshir & et al. (1990)
18.0	0.5142 ± 0.0210	AKARI	-	0.4941 ± 0.0091	...	Ishihara et al. (2010)
23.7	0.3156 ± 0.0032	MIPS	PSF fit	0.2860 ± 0.0053	29.9 ± 5.3	K. Su, private communication
25.0	0.2923 ± 0.0220	IRAS	-	0.2567 ± 0.0047	...	Moshir & et al. (1990)
60.0	0.1967 ± 0.0110	IRAS	-	0.0442 ± 0.0008	...	Moshir & et al. (1990)
71.4	0.1707 ± 0.0081	MIPS	PSF fit	0.0311 ± 0.0006	140.3 ± 8.8	K. Su, private communication
70.0	0.171 ± 0.0087	PACS	Aperture	0.0311 ± 0.0006	139.5 ± 8.8	This work
100.0	<0.4767	IRAS	-	0.0157 ± 0.0003	...	Moshir & et al. (1990)
100.0	0.1484 ± 0.0077	PACS	Aperture	0.0157 ± 0.0003	132.7 ± 7.8	This work
160.0	0.1343 ± 0.0141	PACS	Aperture	0.0064 ± 0.0001	127.9 ± 14.1	This work
250.0	0.0525 ± 0.0065	SPIRE	PSF fit	0.0024 ± 0.0000	50.0 ± 6.5	This work
350.0	0.0235 ± 0.0080	SPIRE	PSF fit	0.0012 ± 0.0000	22.2 ± 8.0	This work
500.0	0.0167 ± 0.0059 [b]	SPIRE	Aperture	0.0006 ± 0.0000	...	This work

[a]This is the observed flux at γ Dor's position.

[b]Although there is a 3 σ detection at γ Dor's position at 500 μm, the flux is listed as un upper limit since there is a known background source within the 500 μm beam.

Note. — The fluxes compiled from the literature and determined in this work for γ Dor are listed. We list the method that is used for the hitherto unpublished flux measurements (*Herschel* fluxes from this work and MIPS fluxes from K. Su, private communication) and the excess that is inferred from them.

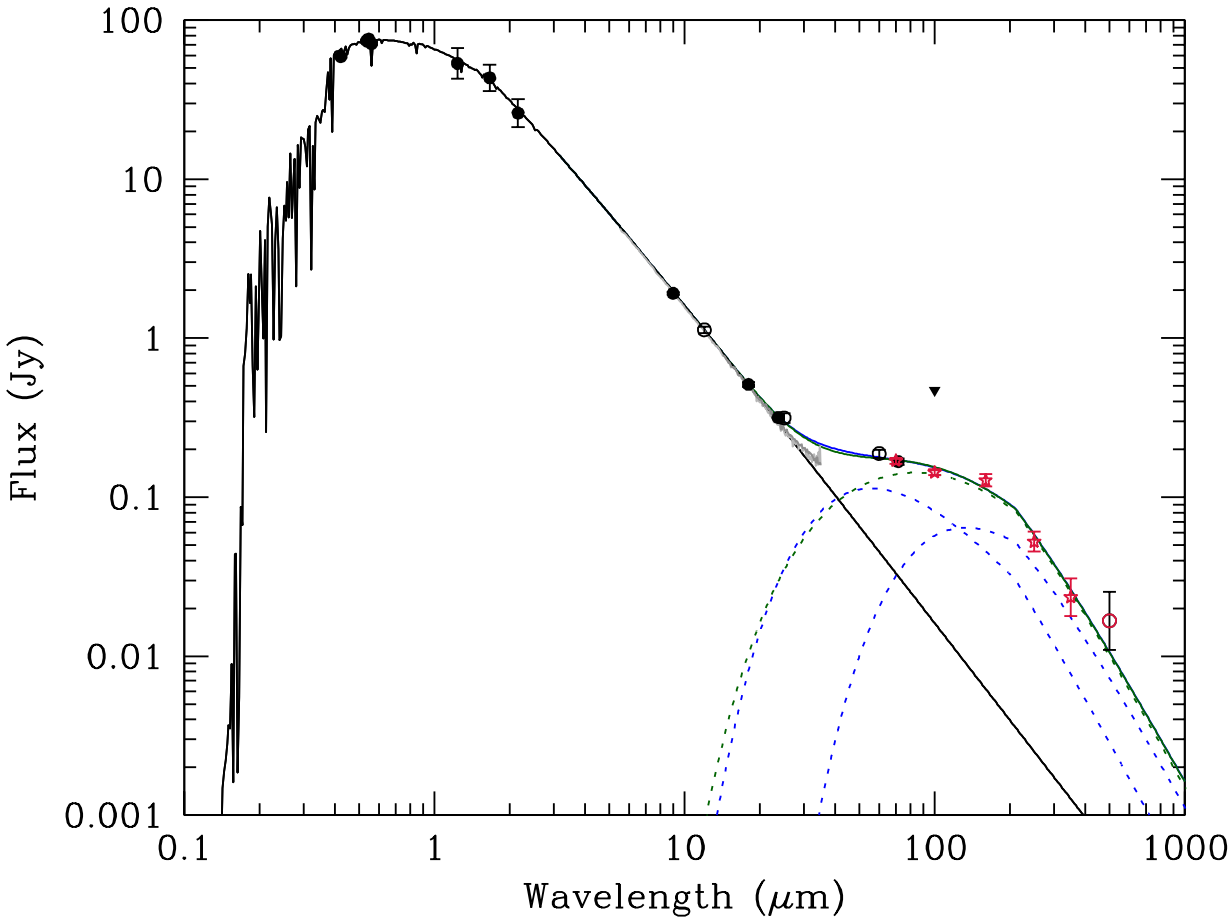

Figure 4.1 The *black line* traces the photospheric model. The narrow rings and the wide ring disk models are plotted in *blue* and *green*, respectively. The *dashed coloured lines* trace the flux originating from the disk and the *solid coloured lines* trace the total flux of the model for the star and disk system. Fluxes from this work are displayed with *red stars*. *Circles* represent archival data. Fluxes which contain a contribution from a background source, *IRAS* fluxes and our 500 μm flux, are displayed with *open circles*. (These fluxes are not included in the SED modelling.) Upper limits are shown with *triangles*. IRS spectra are displayed in *grey* for comparison only and are not included in the SED modelling.

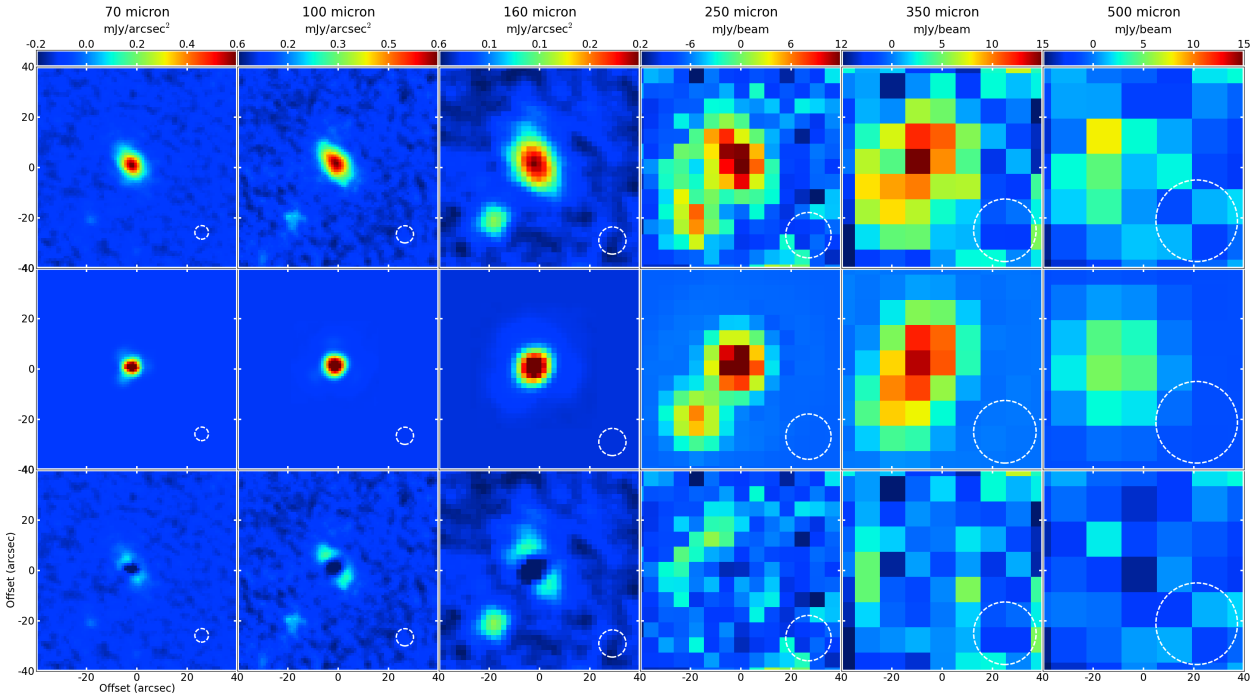

Figure 4.2 The observations *(top panels)*, the fitted PSFs to the star and disk system *(middle panels)* and their residuals *(bottom panels)*. At SPIRE wavelengths two PSFs are fit simultaneously to γ Dor and the background source by fixing their positions according to the fitted PSFs at 160 μm. Clearly γ Dor is not well modelled by a PSF at 70, 100 or 160 μm. The extended nature of the disk is evident in the residuals. The PSF fit at 250 and 350 μm on the other hand can be used to measure the flux of both γ Dor and the background source. The fitted PSF at 500 μm includes both γ Dor and the nearby background source. Beam sizes (FWHMs of the PSFs) are shown in the bottom right corners.

Table 4.3. Position of fitted PSFs to γ Dor in PACS and SPIRE maps

Wavelength (μm)	Coordinates on observation date	Fitted sky coordinates	Offset ($''$)
100	4:16:1.699, -51:30:49.953	4:16:1.461, -51:30:51.824	2.2
160	4:16:1.699, -51:30:49.953	4:16:1.453, -51:30:51.997	2.4

4.2.1 PSF fitting

Observations of the diskless star α Boo are reduced in the same manner as the DEBRIS data and used as the instrumental PSF for PACS data. SPIRE PSFs are downloaded from the ESA ftp site.[2] The target is fit with a PSF by rotating the instrumental PSF to match the rotation of the telescope at the time of the observations. The flux and the stellar position are left as free parameters. The 160 μm PSF is composed of two equally weighted PSFs, each rotated to a different position angle according to the rotation of the telescope during each observation. The stellar position must be left as a free parameter in the PSF fit because of *Herschel*'s 2.3″ pointing error and because the peak of the emission from the star and disk need not be at the stellar position.

PSFs are fit to both γ Dor and the south-east background source at PACS wavelengths. (The identification of background sources is discussed in Appendix A.) The residuals shown in Figure 4.2 indicate that γ Dor is clearly resolved at 70, 100 and 160 μm and resolved along its long axis at 250 μm. The PSF misses the extended structure along the northeast-southwest direction. There is also a hole in the centre of the PSF position in the residuals since the peak of the PSF is overestimated to account for the significant amount of emission on larger scales. The background source on the other hand is well described by the fitted PSF which is used to estimate its flux. (Refer to Table A.1 for the fitted flux of the background source in the *Herschel* maps.)

At SPIRE wavelengths the background source is no longer well-separated from γ Dor as it was at PACS wavelengths. For this reason it is necessary to fit two PSFs simultaneously to the stellar position and the position of the background source. These coordinates are determined from the PSF fits to the 160 μm map, as the objects are both well separated and sufficiently bright at this wavelength to confidently measure their positions. Only the fluxes of the PSFs are left to vary in the fits to the SPIRE maps. The positions of the PSFs fit to γ Dor are listed in Table 4.3 along with any offsets from the stellar position. The fitted PSFs are shown in Figure 4.2 along with the residuals after they are subtracted from the map.

[1] Colour corrections are taken from the SPIRE Observer's Manual v2.4 to account for the slope of the SED through the filters.

[2] ftp://ftp.sciops.esa.int/pub/hsc-calibration/SPIRE/PHOT/Beams/)

Table 4.4. Apertures used to determine PACS fluxes

Band (μm)	Semi-major axis (arcsec)	Eccentricity	Position Angle (°)	Flux (mJy)
70	30	0.780	56	142.6 ± 1.6
100	30	0.820	52	142.6 ± 1.6
160	30	0.750	62	135.2 ± 1.6

Note. — The quoted uncertainty is the quadratic sum of the individual pixel errors within the aperture.

4.2.2 Point source subtraction

The PSFs that are fit to γ Dor and the background source are used to create source-subtracted maps of the dust around γ Dor (shown in Figure 3.3). The stellar photospheric model is subtracted from the map by scaling the fitted PSF to the expected photospheric flux at each wavelength. (The fitted PSF is being used to determine the position of the target which is consistent within *Herschel*'s 2.3″ pointing error (Observer's Manual version 4). The contribution from the background source is also removed by subtracting its fitted PSF from the map. The source-subtracted maps in Figure 3.3 show that the emission is less centrally peaked (and still extended) without the stellar contribution and that the disk is the dominant source of emission in these maps. Subtracting the stellar contribution has a negligible effect on the SPIRE maps as the expected photospheric flux is so low at these wavelengths.

4.2.3 Aperture photometry

Aperture photometry at 70, 100, 160 and 250 μm is used to determine the flux of the γ Dor system as the disk is too extended at these wavelengths for PSF fitting to provide an accurate measurement (especially in PACS maps). Elliptical apertures are used to match the observed shape of the disk. Their properties, which are defined by the 2D Gaussian fits in Section 4.2.4, are listed in Table 4.4. We use maps where the PSF model of the background source has been subtracted.

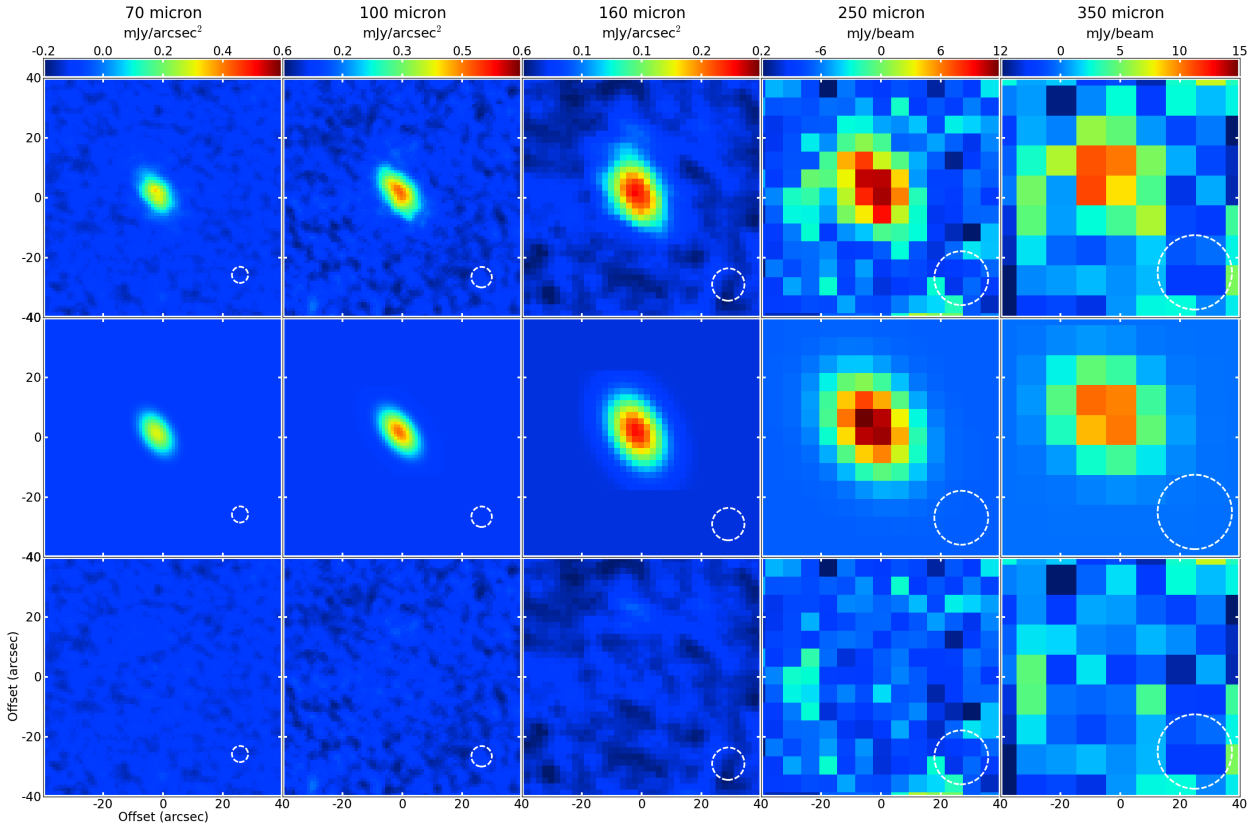

Figure 4.3 The star-subtracted maps *(top panels)* are modelled with 2D Gaussians *(middle panels)* in order parametrize the disk at 70, 100, 160, 250 and 350 μm *(left to right)*. The residuals are also shown *(bottom panels)*. Beam sizes are shown in the bottom right corners.

4.2.4 2D Gaussian fits

2D Gaussians are fit to the γ Dor observations both before and after removing the stellar photospheric model at 70, 100 160 and 250 μm to characterize the structure and extent of the emission. The central position, the position angle, the major Full Width at Half Maximum (FWHM), the minor FWHM, and the peak flux value are left as free parameters. The fitted parameters are used to estimate the size of the disk (characterized by the major FWHM), to measure its orientation (position angle and inclination) and to define the elliptical annuli used to measure surface brightness distributions (Section 4.3). As noted in Section 4.2.1 the centre of the Gaussian is left as a free parameter as the centre of the disk need not coincide with the stellar position. The position of the 2D Gaussian model is consistent with the position of γ Dor within *Herschel*'s 2.3″ pointing error. The 2D Gaussian models provide an

Table 4.5. 2D Gaussian fits

Band (μm)	Object	Beam ($''$)	FWHMs major ($''$)	FWHMs minor ($''$)	Deconvolved FWHM major ($''$)	Deconvolved FWHM minor ($''$)	Inclination[a] ($^\circ$)	Position Angle ($^\circ$)
070	disk	5.6	12.7 ± 1.1	7.9 ± 0.8	11.4 ± 1.2	5.6 ± 1.1	60.5 ± 10.1	58.4 ± 8.0
100	disk	6.7	14.2 ± 0.9	8.2 ± 0.6	12.5 ± 1.0	4.7 ± 1.1	68.1 ± 7.4	51.8 ± 6.4
160	disk	11.0	20.2 ± 1.7	13.3 ± 0.7	16.9 ± 2.1	7.5 ± 1.4	63.7 ± 9.1	61.5 ± 7.2
250	disk	18.0	26.3 ± 7.3	19.3 ± 6.1	19.2 ± 10.1	– [b]	– [b]	55.2 ± 32
350	disk	25.0	27.7 ± 11.9	22.7 ± 7.6	– [c]	– [c]	– [c]	– [c]
070	star+disk	5.6	10.2 ± 1.3	7.3 ± 0.6	8.6 ± 1.6	4.7 ± 0.9	57.0 ± 15.6	55.7 ± 14.3
100	star+disk	6.7	12.7 ± 0.9	7.9 ± 0.6	10.8 ± 1.1	4.1 ± 1.2	67.5 ± 9.5	51.9 ± 7.2
160	star+disk	11.0	19.2 ± 1.4	13.1 ± 0.8	15.7 ± 1.8	7.0 ± 1.6	63.4 ± 10.1	61.7 ± 8.6
250	star+disk	18.0	26.0 ± 7.5	19.1 ± 5.9	18.8 ± 10.5	– [b]	– [b]	55.7 ± 32
350	star+disk	25.0	27.5 ± 11.1	22.8 ± 7.9	– [c]	– [c]	– [c]	– [c]

[a]Calculated using deconvolved disk sizes.

[b]The disk is only resolved along one axis at 250 micron, therefore the inclination cannot be calculated at this wavelength.

[c]The system is consistent with being unresolved and symmetric at this wavelength.

Note. — γ Dor's disk appears larger at longer wavelengths. The errors from the χ^2 minimization fit and the errors from determining an acceptable parameter range (Section 4.2.4) are added in quadrature. The errors from the χ^2 fit are negligible in comparison the uncertainty in the parameter range that can be fit to the data. These are not calculated at 350 μm since γ Dor's emission is consistent with a PSF. Subtracting stellar flux has a negligible effect on the 2D Gaussian fits at longer wavelengths since it is so low in comparison to the disk flux at these wavelengths.

independent assessment of whether the dust is resolved. This is indicated by a 2D Gaussian's FWHM that is larger than the FWHM of the PSF at that wavelength.

The 2D Gaussian models of the star-subtracted images and their residuals are shown in Figure 4.3. These models are used to characterize the observed spatial distribution of the disk's emission since the modelled contributions from all other sources in the vicinity have been removed. The major and minor FWHMs are deconvolved from the beam size (listed in Tables 3.1) using

$$\theta^2_{observed} = \theta^2_{actual} + \theta^2_{beam} \tag{4.1}$$

where θ_{actual} is the actual angular size of the object, θ_{beam} is the effective beam size and $\theta_{observed}$ is the observed angular size of the object. We assume that the true shape of the disk is circular and thus the disk appears elliptical because it is inclined to the line of sight. Therefore the FWHM of the major axis describes the extent of the disk and the FWHM of the minor axis its projection. We use the ratio of the deconvolved major and minor FWHMs to estimate an inclination of $\sim$65° from a face-on orientation. Our measurements are consistent an inclination of $\sim$70° for γ Dor based on the analysis of star's oscillation modes (Balona et al., 1996).

Estimating the errors on the 2D Gaussian models

The errors on the fitted parameters of the 2D Gaussian models are estimated by varying the parameters around the fitted value and inspecting the residuals. We quote the range of parameter values for which the absolute sum of the residuals changes by less than 10%. This threshold is biased to the size of the map because a larger map area increases the absolute sum of the residuals. Therefore, we use the small area around the disk to maximize the fraction of residual map that it covers. We also look at the same area on the sky between the residual maps we compare. Figure 4.4 shows an example of the model, residuals and histogram of the residuals for the disk emission at 100 μm (source-subtracted map, Section 4.2.2). The threshold of a 10% change is used for all maps at all wavelengths for consistency. The residual maps are inspected visually to ensure the resulting parameter error range is reasonable and therefore that the 10% threshold is also reasonable.

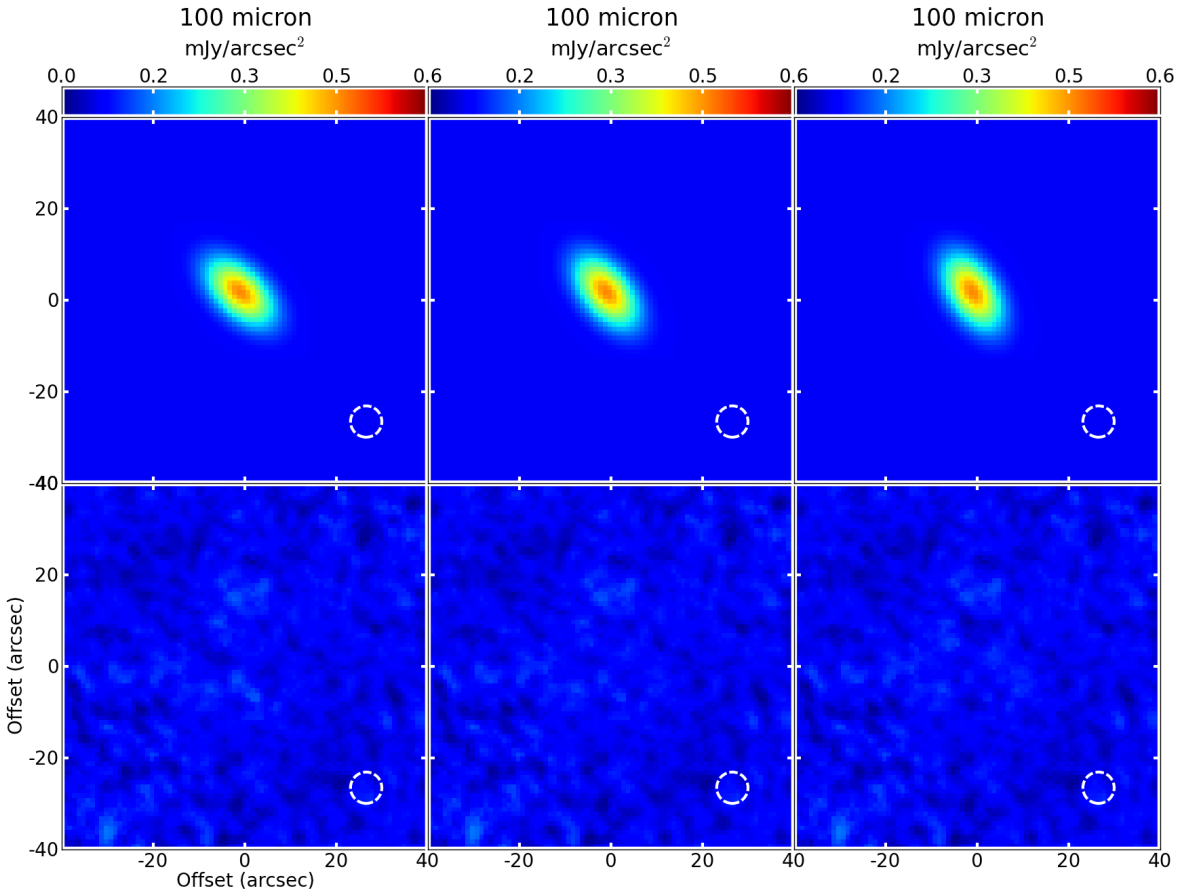

Figure 4.4 Example of an acceptable range in the fitted value of the position angle at 100 μm for the 2D Gaussian disk model. The model with each parameter value *(top panels)* and its residuals *(bottom panels)* are shown for models with a position angles of 44.6°, 51.5°and 57.5° *(left to right)*.

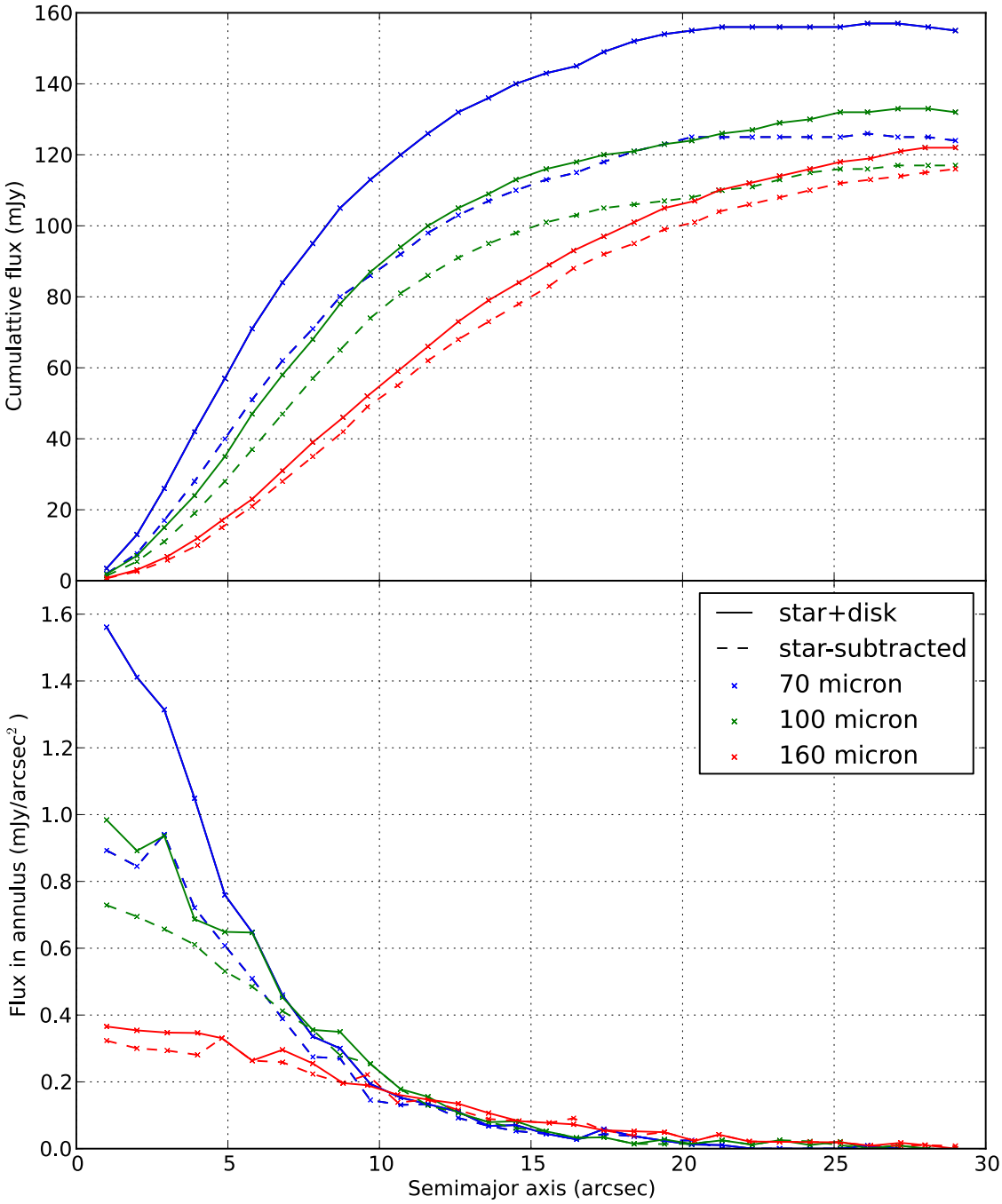

Figure 4.5 The cumulative flux *(top panel)* and average flux *(bottom panel)* enclosed in elliptical annuli with increasing semi-major axis at 70 *(blue)*, 100 *(green)* and 160 *(red)* μm. The profiles of the star and its disk *(solid lines)* are shown. The stellar model is subtracted from the maps to measure the profile of the disk only *(dashed lines)*. (The model of the nearby background source is also subtracted from the maps.) It is evident that the stellar contribution to the flux declines at longer wavelengths. The central peak in brightness of the the dust also declines at longer wavelengths, but the dust profiles at each wavelength converge at a semi-major axis of $\sim$10$''$. This implies that the dust distribution appears to have the same size at all wavelengths.

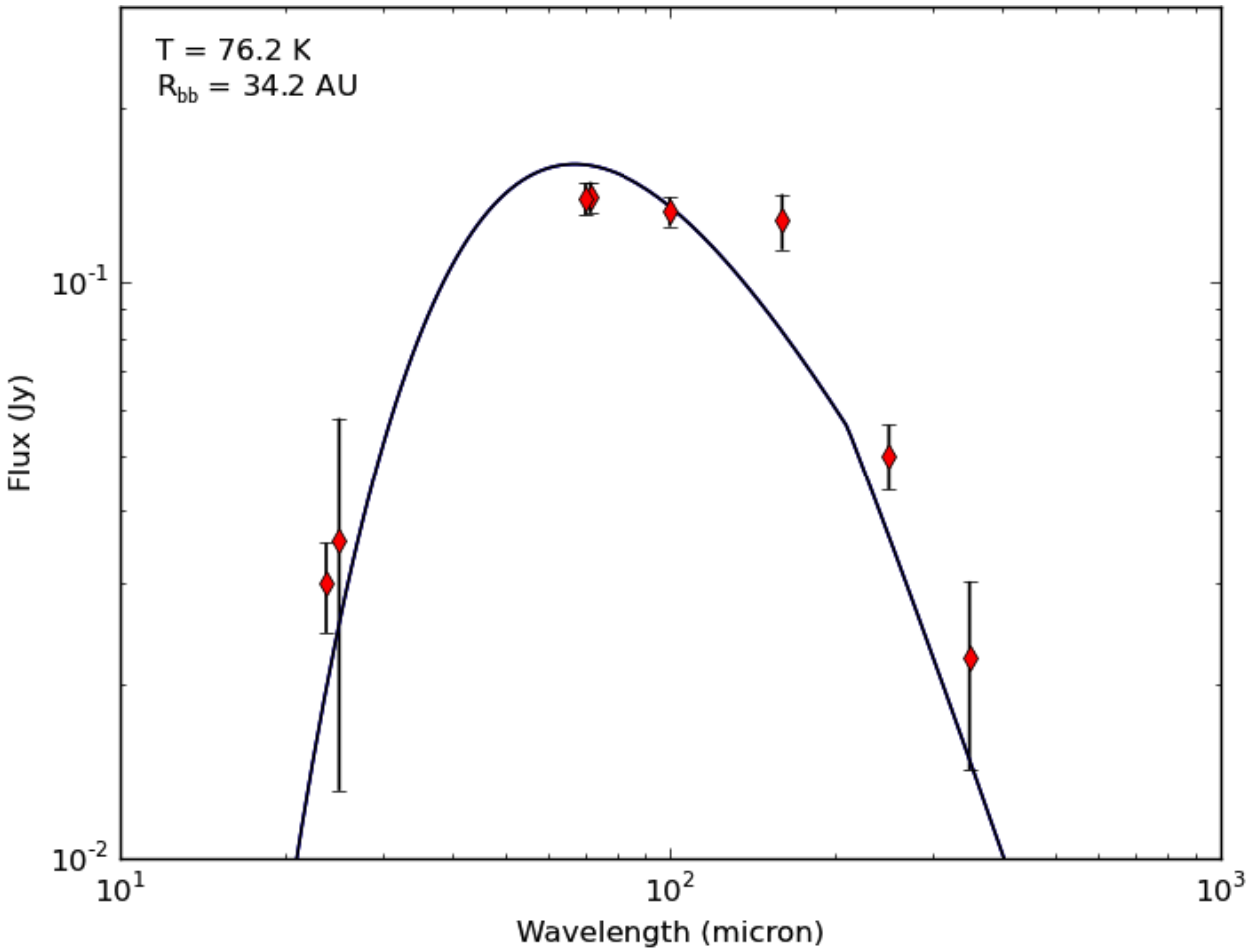

Figure 4.6 The SED of γ Dor's disk is quite broad and cannot be fit with a single temperature. Therefore models that incorporate a range of temperature are investigated in Sections 4.4.1 and 4.4.2.

4.3 Surface Brightness Distributions

We measure how the brightness of the system changes as a function of distance from the star. We use the 2D Gaussian models (Section 4.2.4) to define the position angle, ellipticity, and centre of the elliptical apertures. We use apertures of increasing semi-major axis to measure the surface brightness profiles at 70, 100 and 160 μm. The cumulative flux and surface brightness distributions (Figure 4.5) show a smoothly declining disk with no evidence of rings or bumps in the dust's radial distribution.

4.4 SED modelling

The SED of the excess emission is analyzed to model the dust. The first approach is to assume that the dust grains emit as blackbodies, as discussed in Section 1.2.1. Even though this may not be a realistic assumption, it does provide some initial constraints on the disk properties and a simple method of comparing known debris disks to each other. This approach determines disk sizes that are typically a factor of 2-3 smaller than the observed sizes of disks (Matthews et al., 2010; Wyatt, 2008, and references therein) because a lower radiation efficiency of the grains, dependent on their size and composition, will make them appear hotter than blackbody grains at the same distance.

In order to include a more realistic representation of how dust grains emit in debris disks to reproduce the observed SEDs, we modify the blackbody function by a factor $X_\lambda = (\lambda/\lambda_0)^\beta$ at wavelengths longward of λ_0 (Dent et al., 2000). This accounts for the observed fall off of the spectrum that is steeper than the blackbody function at submm wavelengths. λ_0 and β can be constrained by the SED, however here we adopt $\lambda_0 = 210$ μm and $\beta = 1$, as is commonly found for debris disks because we are limited by our sampling of the SED to constrain these.

The majority of debris disk SEDs can be modelled with a single temperature blackbody function (see discussion in Section 2 of Wyatt, 2008) and more sophisticated models incorporating dust composition and grain sizes can be developed when necessary to reproduce the shape of the SED. The broadness of the SED can also be accounted for by incorporating a range of temperatures within the disk. This can be due to a range of locations of the dust or a range of dust properties.

γ Dor's excess has a broad SED that cannot be described by a single temperature (see Figure 4.6). Therefore it is modelled with a range of temperatures. First, in Section 4.4.1, a model of two narrow rings at different radii from the star is used. Each ring is represented by a modified blackbody function. In Section 4.4.2, the disk is modelled as a continuous distribution of dust (with power law-temperature distribution and a power law surface density distribution that both fall off at further distances from the star). We fit these models using the χ^2 minimization package MPFIT.

IRAS photometry at 25 and 60 μm is not used when fitting the SED because the large beam of *IRAS* is more likely to include nearby background sources in the flux measurement. Moreover, this photometry is not needed as MIPS photometry

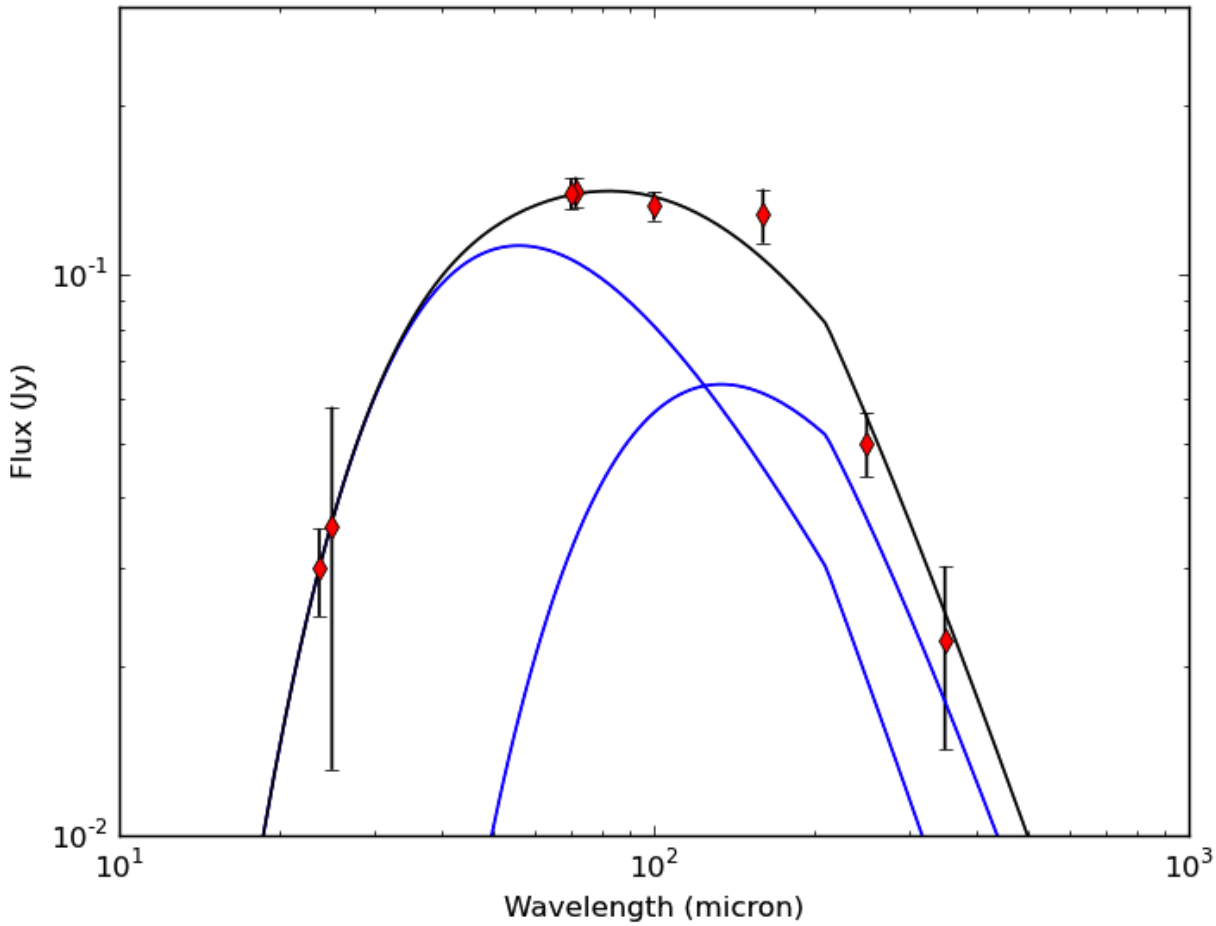

Figure 4.7 The disk emission *(red diamonds)* is modelled by two narrow rings with temperatures of ∼90 and 35 K corresponding to blackbody radii of ∼25 and 135 AU, respectively. The models of the individual narrow rings *(blue lines)* predict the total flux observed from the dust *(black line)*.

at 24 and 70 μm is available for this source and samples the SED at comparable wavelengths. (PACS 70 μm data is also available.) The *IRAS* fluxes are either higher than or consistent with MIPS. The *IRAS* upper limit at 100 μm is not used as the target is detected at 100 μm with PACS. The IRS data are not used in the SED modelling, but a comparison of the results to those data reveal that they are consistent within ∼10%, which is expected when comparing IRS data to photometric data.

Table 4.6. A possible narrow ring model for γ Dor's disk

Parameter	Units	Inner ring	Outer ring	Total
Temperature	K	91 ± 35	38 ± 47	–
Radius	AU	24 ± 18	136 ± 336	–
$\sigma(R)$	AU^2	0.14 ± 0.25	1.08 ± 0.57	
Dust mass	10^{-3} $M_\oplus$	0.8 ± 1.0	5.9 ± 3.1	6.7 ± 3.4

4.4.1 Narrow rings

The dust emission is fit with a modified blackbody function (Dent et al., 2000),

$$F_\lambda = 2.35 \times 10^{-11}\ d^{-2}\ \sum_R\ \sigma(R)\ B_\lambda(\lambda, T(R))\ X_\lambda^{-1} \tag{4.2}$$

where F_λ is the flux density (in Jy) at wavelength λ (in μm), d is the distance to the star (in pc) and $\sigma(R)$ is the cross-sectional area (in AU^2) of the ring at radius R (in AU). $B_\nu(\lambda, T(R))$ is the Planck function (in Jy) for the ring at radius R with temperature T (in K) given by

$$B_\lambda(\lambda, T(R)) = \frac{2hc^2}{\lambda^5} \frac{1}{\exp(\frac{hc}{\lambda k_B T}) - 1} \tag{4.3}$$

where h is the Planck constant, c is the speed of light, and k_B is Boltzmann's constant. Equation 4.2 is modified by X_λ, where $X_\lambda = (\lambda/\lambda_0)^\beta$ for wavelengths longer than λ_0 and $X_\lambda = 1$ otherwise. Recall that we adopt $\lambda_0 = 210$ μm and $\beta = 1$, as is commonly found for debris disks (Dent et al., 2000).

Each modified function represents a narrow ring, the blackbody radius of which is calculated from its temperature using

$$R = 278.3^2\ L_*^{1/2}\ T^{-2} \tag{4.4}$$

The fitted parameters are listed in Table 4.6. Figure 4.7 shows the SED model with the observed fluxes. The model does not reproduce the 160 μm flux well. The adoption of $\lambda_0 = 210$ μm and $\beta = 1$ agrees well with the shape of the SED: β accounts for the slope of the spectrum between 250 and 350 μm points, while $\lambda_0 = 210$ μm in the 160 - 250 μm range is preferred. If λ_0 were longer than 250 μm the model would not be able to account for both the 250 and 350 μm fluxes. A λ_0 shorter than 160 μm would result in an over-prediction of not just the 160 μm flux, but of fluxes at shorter wavelengths as well.

4.4.2 Wide ring

The wide ring model is merely an extension of the two-component model in Section 4.4.1. Instead of using two discrete rings that are represented by two blackbody functions, the wide ring is represented by a continuous distribution of blackbody func-

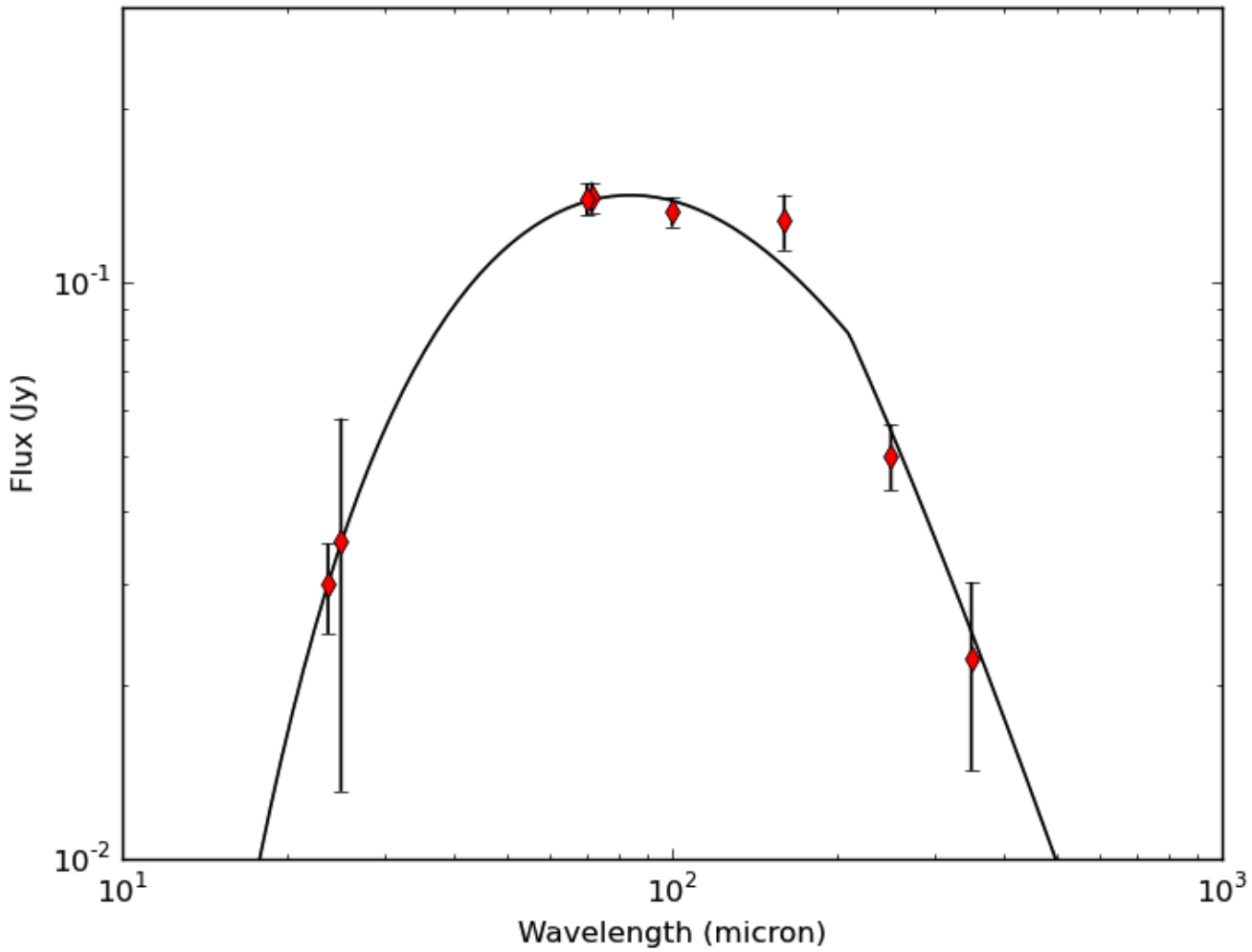

Figure 4.8 The excess *(red diamonds)* is modelled by a wide ring extending from ∼15 to 230 AU predicting the total flux observed from the dust *(black line)*.

Table 4.7. A possible wide ring model for γ Dor's disk

Parameter	Units	Value
R_{in}	AU	15 ± 10
R_{out}	AU	230 ± 270
γ	–	-0.71 ± 1.0
σ_{total}	AU^2	29 ± 4
Dust mass	$M_\oplus$	6.7×10^{-3}

tions. We use Equation 4.2 with σ and T distributed according to power laws. The cross-sectional area is determined from the cross-sectional area per AU^2, $\Sigma(R)$, given by,

$$\Sigma(R) = \Sigma_0 \; R^{-\gamma} \tag{4.5}$$

where Σ_0 is the cross-sectional area per AU^2 in the innermost region of the disk and γ describes the fall off of the surface density at further distances from the star. Similarly, $T(R)$ is given by,

$$T(R) = T_0 \; R^{-\delta} \tag{4.6}$$

where T_0 normalizes the temperature distribution and δ describes how quickly the temperature of the dust grains declines at larger radii from the star. As in Section 4.4.1, we treat the dust grains like blackbodies by adopting $\delta = 0.5$ and $T_0 = 438.4$ K according to Equation 4.4. This allows the results to be directly compared to the results in Section 4.4.1, the resolved images, and other debris disks. The resulting model is shown in Figure 4.8 and its fitted parameters are listed in Table 4.7.

4.4.3 Disk mass

The dust mass is measured by summing up the mass of each dust ring by

$$M_{dust} = \sum_R \; M_R = 4.26 \times 10^{10} \; d^2 \; \sum_R \; F_{\lambda,R} \; B_\lambda(T_R, \lambda)^{-1} \; \kappa_\lambda^{-1} \tag{4.7}$$

where M_R is the mass of each ring (in $M_\oplus$), $F_{\lambda,R}$ is the flux of that ring at λ (in Jy) and T_R is the temperature of the ring (in K). (The other parameters are defined with Equation 4.2.) $\kappa_{850\mu m} = 45$ AU^2 $M_\oplus^{-1}$ is adopted to be consistent with and compare to other studies (Najita & Williams, 2005; Williams & Andrews, 2006). Therefore the expected flux at 850 μm for each ring is extrapolated from the model to calculate a dust mass of $6.7 \times 10^{-3} M_\oplus$ for both the narrow rings model fit described in Section 4.4.1 and the extended ring model in Section 4.4.2.

From the dust mass we can approximate the fractional luminosity from Equation 7 in Wyatt (2008)

$$M_{dust} = 12.6 \; f \; R^2 \; \kappa_\lambda^{-1} \; X_\lambda^{-1} \tag{4.8}$$

which yields a fractional luminosity of $\sim 2.5 \times 10^{-5}$ for both the narrow rings model and the wide ring model.

Chapter 5

Discussion & Conclusions

5.1 Comparing SED models: unresolved fluxes

The total emission of both SED models (Figures 4.7 and 4.8) has a similar shape. Both models reproduce all the observed fluxes well, except for the 160 μm flux. Therefore we cannot favour one model over the other based on the SED alone. Typically, models of multiple narrow rings are justified if a deficit of flux is observed in the SED between components, however, no such deficit is evident in the SED of γ Dor's disk.

Neither the narrow rings model nor the wide ring model can account for the observed 160 μm flux. Both debris disk *Herschel* Key Programmes (DEBRIS and DUNES) have found a number of disks which have a higher 160 μm flux than expected (Krivov et al., in prep.). If this feature is verified, it will have to be explained by the dust models. If it were not for *Herschel* submillimetre fluxes that constrain the coldest dust temperatures, the SED modelling presented here would compensate for the 160 μm flux with a colder, more massive disk component. As an example of this, Figure 5.1 shows the resulting model when the SPIRE fluxes are excluded. The radius of the outer component is more than a factor of 2 larger than that for the model in Figure 4.7. Comparisons with other SPIRE imaged disks would reveal whether they also show this excess 160 μm flux because *Herschel*'s sensitivities in this wavelength range are unprecedented and therefore better constrain the decline of the SED.

A β value larger than the adopted value of 1 could also compensate for some of the 160 μm flux, as it steepens the slope of the SED in the submillimetre even more. An example is shown in Figure 5.2 where the steeper slope is still within the uncertainties of the SPIRE data but now is also within the uncertainties at 160

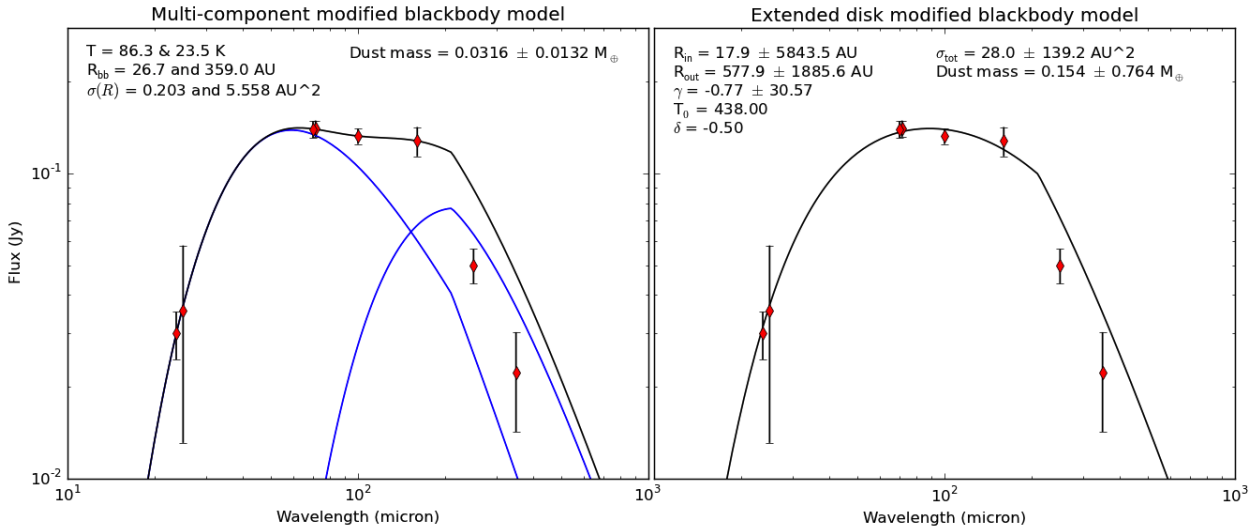

Figure 5.1 **Note: for demonstration purposes only.** An example of how a colder disk component could be used to account for a large 160 μm flux. If it were not for the SPIRE fluxes, the outer extent of the dust could not be constrained.

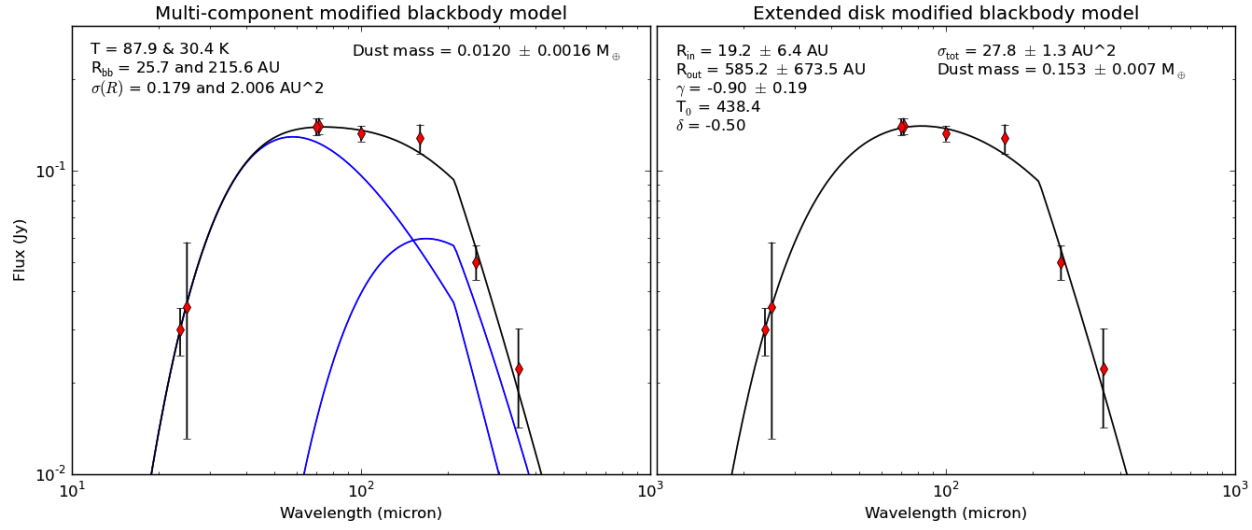

Figure 5.2 **Note: for demonstration purposes only.** An example of how varying the slope of the SED in the submillimetre could account for a large 160 μm flux. The SED model with this modification still lies within the uncertainties of the SPIRE data but now also agrees with the PACS 160 μm data. Observations at longer wavelengths could help constrain the slope.

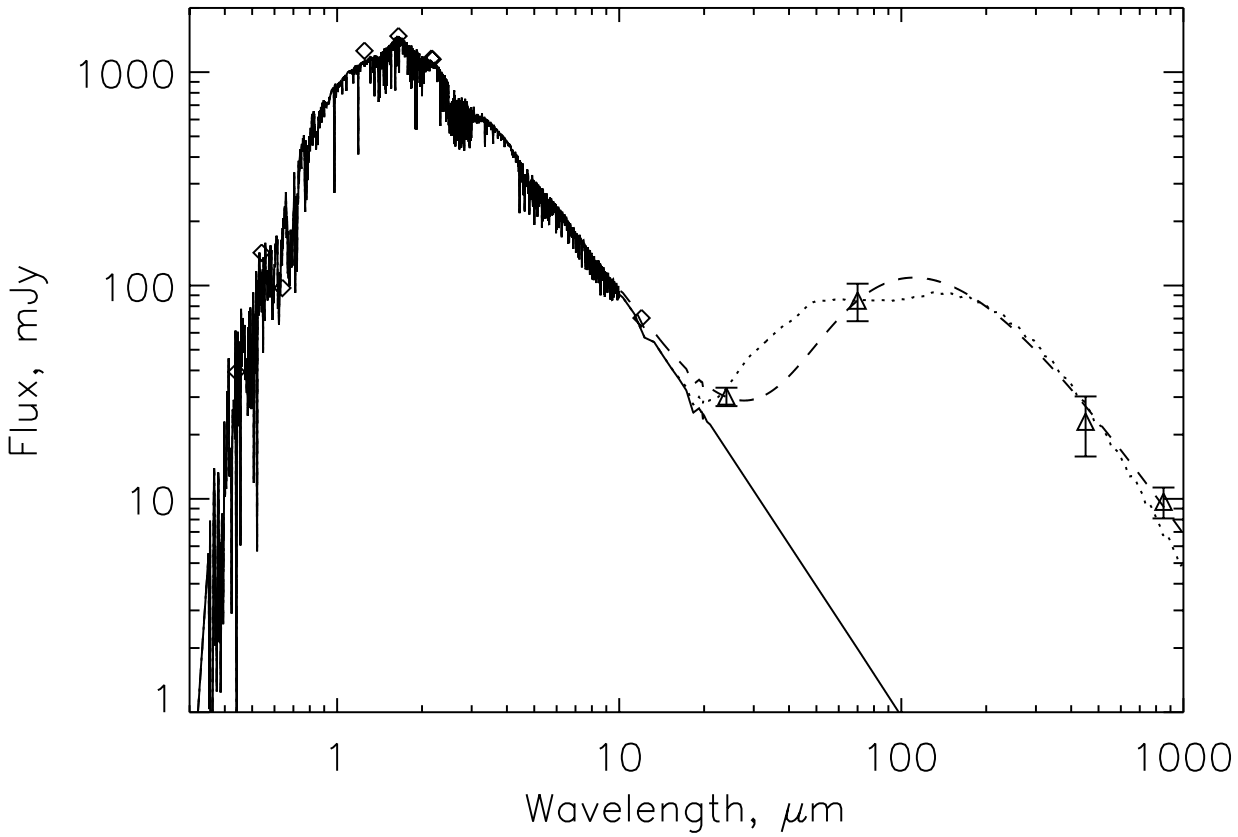

Figure 5.3 Figure 2 from Matthews et al. (2007) for the debris disk around TWA 7 showing that that a range of temperatures in a disk can be explained by both dust at the same location with a range of grain sizes *(dotted line)* or dust at a range of distances from the star *(dashed line)*. The peak of the SED model with a range of dust grain sizes is quite flat in comparison to the model of dust at various distances. This model is just one set of parameters that fit the other data.

Table 5.1. Comparing measurements of disk size

Method	Inner extent (AU)	Outer extent (AU)	Convolved size (AU)
Narrow rings	20	140	260
Wide ring	15	230	320
2D Gaussian	–	340	400

Note. — Comparisons for the observed extent of the dust at 160 μm. *Herschel*'s effective beam size at 160 μm of 11″ has been used to compare convolved and deconvolved sizes using Equation 4.1.

μm. This modification could be justified if data at wavelengths longer than SPIRE wavelengths were available to constrain the submillimetre slope.

The flatness of the SED across PACS wavelengths (70-160 μm) is not characteristic of blackbody emission and and so the properties of a debris disk that can be responsible for this should be investigated further. For example, Matthews et al. (2007) model the dust in the debris disk around TWA 7 with a range of grain sizes. The peak of this model's SED is flat in comparison to their model of dust at a range of distances from the star (shown in Figure 5.3). A similar model could be investigated for γ Dor in the future.

5.2 Breaking degeneracies in SED modelling

Preferred SED model: As discussed in Section 5.1, it is not clear whether one SED model of unresolved fluxes is preferred over the other. The resolved images, however, show smoothly declining emission at further distances from the star. Modelling the observed emission with a 2D Gaussian shows no evidence of discrete components in the residuals (Figure 4.3). Furthermore, the narrow rings model in Figure 4.7 implies that the ring at 20 AU (1″) dominates the image at 70 μm and the ring at 140 AU (7″) dominates the 160 μm image. This is not characteristic of the centrally peaked emission that is observed at 70, 100

and 160 μm in maps (see Figures 4.3 and 4.5 in particular) since the apparent morphology of the dust does not change at longer wavelengths (as is found for disks with multiple components at different distances like η Corvi: Matthews et al., 2010). The centrally peaked Gaussian-like morphology observed at each wavelength is more characteristic of a wide ring rather than two narrow rings. This issue will be investigated in the future by modelling the images. The image modelling convolves a model of the distribution of emission at each wavelength (based on a model of the geometry and temperature of the disk) with *Herschel*'s beam for comparison with the observed map.

Comparison of disk sizes: Table 5.1 lists the extent of the dust that is estimated from SED models and images. Both SED models underestimate the extent of the disk that is observed. This is consistent with results for other disks (for example, β Leo: Matthews et al., 2010; Churcher et al., 2011). This shows that any image modelling will have to incorporate different grain properties (like composition and size) to reconcile the temperatures from the SED and the spatial distribution from the resolved images.

Dust location: The SED fits require a range of temperatures for the dust in the γ Dor disk (Figure 4.1). Simple scenarios could be dust at a range of radii or dust grains with a range of sizes at a single radius (see Figure 5.3). Resolved imaging at multiple wavelengths is the best way to break this degeneracy because it shows directly the radial extent of the disk. Longer wavelengths are sensitive to cooler grains. If the disk appears to be the same size at all wavelengths it is more likely that the dust grains are all at the same distance from the star but have a range of sizes. However, if the temperature range is due to a spatial distribution of dust, the disk should appear larger at longer wavelengths. We investigate two different spatial distributions according to the observed temperature range and find that the wide ring model better represents the centrally peaked morphology that is observed at multiple wavelengths.

Another possibility is that the dust is at a single radius with a dust grain size distribution. If this were the case, the coldest dust temperatures would correspond to the largest grains, implying that all the dust extends out to scales > 100 AU. In this scenario, the $\sim$90 K dust would be smaller dust grains at the same distance. This would result in a lack of emission closer to the star that should be observable with *Herschel*'s resolution at the PACS wavelengths,

especially for such an inclined disk.

5.3 Assessing asymmetries

It is interesting to look for asymmetries in disk structure because of their implications for planetary systems. Asymmetries such as warps, clumps, and offsets of the disk's centre from the star can be caused by planetary bodies, as discussed in Section 1.2.2. Unfortunately, warps in γ Dor's disk cannot be investigated because the disk is not edge-on and offsets of the disk centre from the stellar position are consistent within *Herschel*'s 2.3″ pointing error.

We assess the symmetry of the dust structure at each wavelength by examining the residuals of each 2D Gaussian model, a symmetric function. However, Figure 4.3 shows no evidence of excesses or deficits of flux in the residuals. Therefore no brightness asymmetries are apparent in γ Dor's disk at *Herschel*'s resolution and observed wavelengths.

5.4 Comparison to other planetary systems

5.4.1 Comparison to debris disks around F stars

The dust mass is derived from the SED models. Both the narrow rings model and the wide ring model estimate a dust mass of 6.7 $\times 10^{-3}$ $M_{\oplus}$. We compare the dust mass for γ Dor to other known disks in Figure 5.4. γ Dor's dust mass lies within a range that is found for other F-type stars. Considering γ Dor's age of 400 Myr (Chen et al., 2006), it is impossible that the dust is primordial in origin. Furthermore, it is likely that the dust is produced in a steady evolution of the system since it does not have an anomalously high dust mass, a signature of a transient event. Following Wyatt et al. (2007), there is a maximum fractional luminosity for Sun-like stars of $f_{max} = 0.16 \times 10^{-3}\ R^{7/3}\ t_{age}^{-1}$, where R is the dust radius in AU and t_{age} is the age of the star in Myr. A transient event is needed to explain a dust luminosity in excess of this. Using the 400 Myr age for γ Dor and the radii of each dust component in the models in Section 4.4, this corresponds to an f_{max} of 0.39 and 1.2 for the narrow rings model and the wide ring model, respectively. This is much higher than the fractional luminosity of 2.5×10^{-5} calculated in Section 4.4.3. Therefore, a transient event is not needed to explain the observed dust mass around γ Dor.

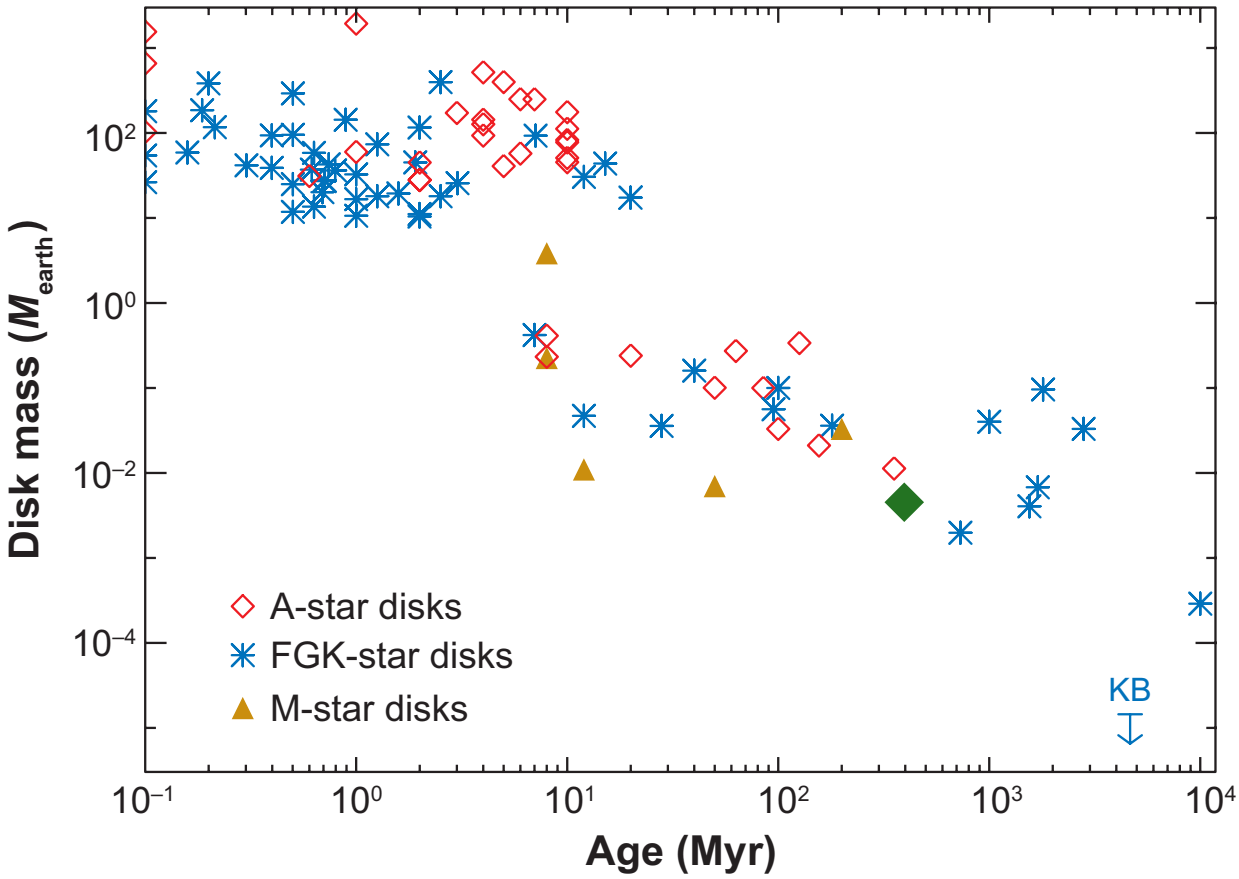

Figure 5.4 Figure 3 from Wyatt (2008) showing observed dust masses of disks around A, F, G, K and M type stars. The dust mass derived from the SED models in Section 4.4, shown by the *green diamond*, lies within the range that is found for F-type stars *(blue asterisks)*.

Given that *Herschel* opens up the parameter space to study cooler and fainter disks (Figure 1.7) γ Dor's disk will be reconsidered in the context of FGK stars surveyed by DEBRIS (Sibthorpe et al. 2012, in prep.).

5.4.2 Relating to planetary systems

γ Dor is an example of how we are continuing to learn more about the structure of debris disks from the improvement in both resolution and sensitivity of modern observatories and moving further from the simple pictures of a single narrow dust rings. There are many debris disks that are known to have multiple dust components, as shown in Figure 5.5. For disks such as the Solar System and HR 8799,[1] planets are observed to lie between the regions of dust. In fact, a planet can clear objects out of its orbit to create these gaps or holes in the disk. In these systems, the debris disk components are the outer-most observed constituents of the planetary system (presumably because planet formation processes become less efficient at large radii, Kenyon & Bromley, 2008). This suggests that gaps in debris disks are good places to look for planets, particularly if the dust ring has a sharp inner edge (e.g., Fomalhaut; Kalas et al., 2005, 2008). If γ Dor's disk is indeed best described by a wide ring with no evidence of discrete components, the best place to look for planets would be within the inner radius of $\sim$20 AU. If there is a giant planet shaping the inner edge of the disk, γ Dor may be a good target for the Atacama Large Millimeter/Submillimeter Array (ALMA) as γ Dor's distance is appropriate to resolve a sharp inner edge. (It is close enough that it is sufficiently bright, but not too close that most of the extended structure is filtered out by the interferometer.)[2]

Although the outer radius of the wide ring model is not well constrained, because of the range of temperatures and declining surface brightness at large radii from the star, the inner radius is well constrained by the warmest dust temperatures present. This is valuable in the context of using the inner edge of the wide ring to determine the locations where planets could possibly lie. In the Solar system, the location of the inner edge of the Kuiper Belt is thought to be determined by the migration of Neptune (Nice model: Levison et al., 2008). Wyatt (2003) present a model that explains the bright clumps (Section 1.1.3) in Vega's disk with the migration of a Neptune-mass planet from 40 to 65 AU over 56 Myr. During the migration, the inner edge of the

[1] An A5V γ Doradus variable star.

[2] This is not feasible for ALMA early science when the array is not operating at it full capacity, but can be re-investigated as more antennas come online.

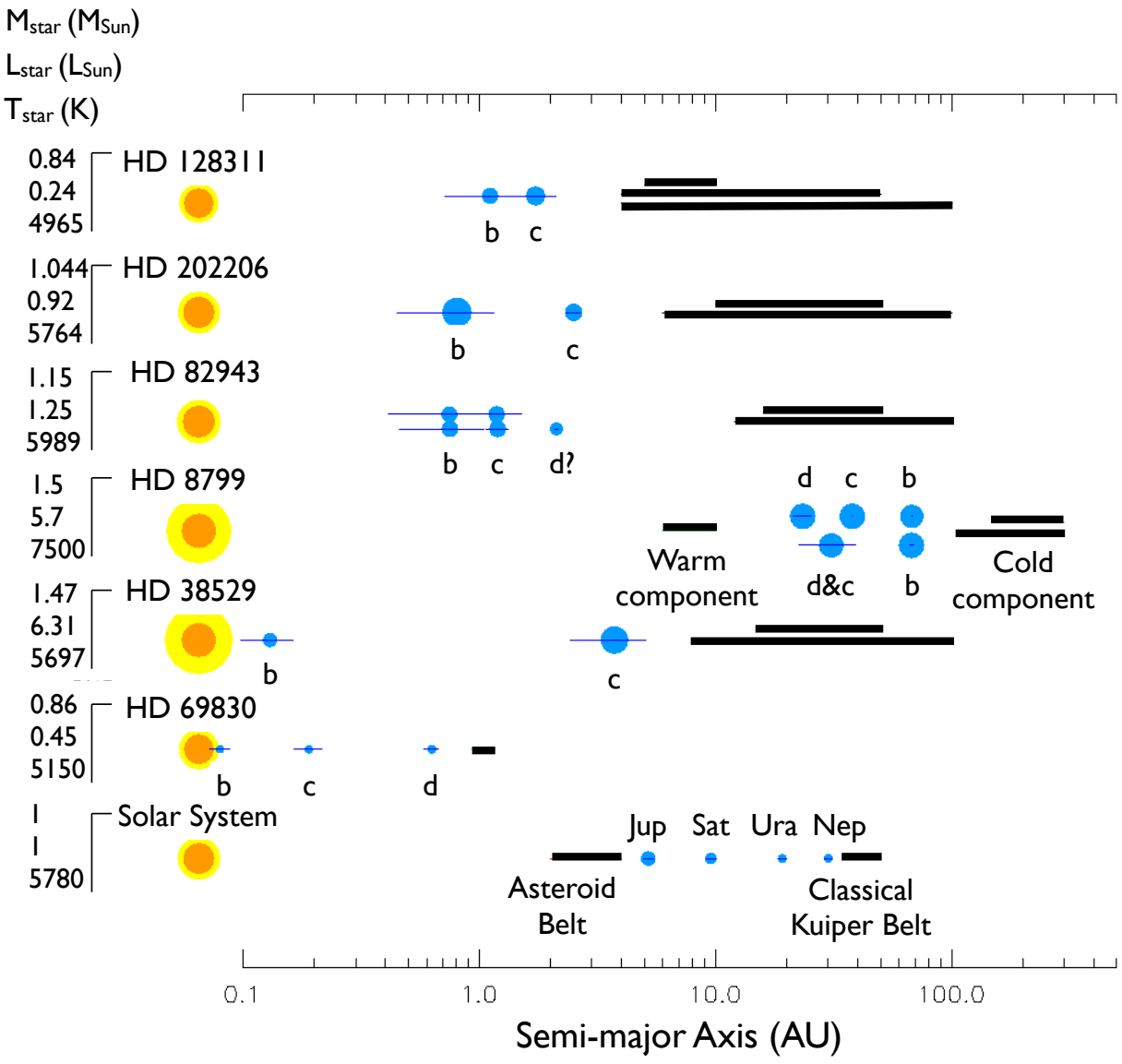

Figure 5.5 The configuration of some known planetary systems consisting of both planets and a debris disk. Planets have been observed to lie in regions inside and between dust components. The different black lines correspond to different possible solutions for the locations of the dust components. *Image credit: Amaya Moro-Martin*

disk is pushed outwards and objects in the disk are swept into resonances with the planet. The structure and location of inner rings can be used to investigate planetary migration in other planetary systems to consider the circumstances present in the Solar system.

Although it would be difficult to observe a planetary system while its planets are migrating, because of the short timescales over which this takes place (on the order of tens of Myr), there are other ways in which the Solar system and its past can be considered in the context of other planetary systems. The Nice model explains the Late Heavy Bombardment (LHB), a massive cratering event responsible for many of the features we still see on the Moon today, as being triggered by the migration of the planets. The LHB bombardment severely depleted the Solar systems debris disk rendering such a system unobservable at the distance of γ Dor within the current detection limits and available observatories (Booth et al., 2009). The observations of debris disks of different ages, particularly ones that are younger than the Solar system, enable study of the likelihood that other planetary systems went through an evolution similar to our own, particularly, a LHB-type event. Although γ Dor is still quite young, the fact that there is so much dust still present suggests that it has not undergone a instability as destructive as the LHB.

Chapter 6

Summary

This thesis establishes the following:

- γ Dor has a debris disk that is resolved by *Herschel* at multiple wavelengths allowing for a comparison of the dust distribution at each wavelength. PSF fits with significant residuals and a comparison of the sizes of the 2D Gaussian models to those of the instrumental PSFs support that the dust is indeed resolved at 70, 100 and 160 μm in both directions. The disk is resolved along its long axis at 250 μm.

- The SED of the dust cannot be modelled with a single temperature. Two SED models that incorporate multiple temperatures are investigated: a model of two narrow rings and a model of a wide ring. The unresolved flux information alone does not indicate whether one model is preferred over the other. Both models fit the data reasonably well with the exception of the 160 μm data which is not explained by either model.

- The extent of the disk estimated from the SED models underestimates the extent that is observed in the resolved images (Table 4.5 and Figure 4.5), taking into account the telescope's resolution. This result has been found for other resolved debris disks (Schneider et al., 2006; Matthews et al., 2010; Churcher et al., 2011; Marshall et al., 2011) and is attributed to the realistic dust grain properties that cause them to emit less efficiently than a perfect blackbody.

- No asymmetries are discernible at *Herschel*'s resolution as shown in the residuals of the 2D Gaussian models (Figure 4.3).

- The morphology of the disk suggests that the dust has a smooth distribution rather than discrete components. The wide ring SED model is therefore a more likely description of this system and can be investigated further with image modelling of the disk.

- The range of temperatures in γ Dor's dust is likely due to a combination of both dust at multiple distances from the star and a range of dust grain sizes. A spatial distribution is necessary to account for the observed 2D Gaussian-like shape of the emission. However, as the morphology of the dust and its spatial extent are independent of wavelength, multiple dust radii alone cannot explain the temperature range.

- The dust mass of 6.7×10^{-3} $M_{\oplus}$ for γ Dor's disk lies within the range that is found for F-type stars of its age. This mass suggests that the dust is generated by steady evolution of the disk rather than a transient event, which would stand out amongst other disks. Furthermore, the fractional luminosity of the dust around γ Dor is within the levels that can be explained by steady state evolution of a debris disk around a Sun-like star of γ Dor's age, described in Wyatt et al. (2007).

Avenues for possible future work include the following:

- An analysis of the SEDs of many debris disks across *Herschel* wavelengths would show whether γ Dor's large 160 μm flux is anomalous. Furthermore SPIRE data toward many debris disks could help determine whether the 160 μm flux is consistently high in comparison to other wavelengths by constraining the fall-off of the SED at long wavelengths.

- Image modelling will investigate whether a model of multiple narrow rings is preferred over a model of a wide ring. It is also necessary to reconcile the discrepancies between the SED models and the resolved images to derive the extent of the dust and shed light on its properties.

- Modelling dust grain size distributions could investigate its effect on the observed temperature range. Such a model should be compared to the results in Matthews et al. (2007) which show a similar SED shape across PACS wavelengths.

- Any sharp features in the disk such as a sharp inner edge or a very narrow ring may be observable with ALMA. A sharp edge could be used to detect a planet shaping it. Furthermore, since ALMA is sensitive enough to detect the photospheres of stars, offsets between the disk centre and the stellar position caused by a planetary companion could also be measured. Both these techniques were used for Fomalhaut with Hubble Space Telescope observations (sharp edge: Quillen 2006, offset: Kalas et al. 2005) and ALMA enables us to do explore this in more systems.

- If one were to look for planets around γ Dor and its disk is indeed a wide ring, regions within the inner radius of 20 AU should be preferentially targeted.

Bibliography

Allard, F., Hauschildt, P. H., Alexander, D. R., & Starrfield, S. 1997, Annual Review of Astronomy and Astrophysics, 35, 137

Andrews, S. M. & Williams, J. P. 2005, Astrophysical Journal, 631, 1134

Andrews, S. M., Wilner, D. J., Espaillat, C., Hughes, A. M., Dullemond, C. P., McClure, M. K., Qi, C., & Brown, J. M. 2011, Astrophysical Journal, 732, 42

Archibald, E. N. et al. 2002, Monthly Notices of the RAS, 336, 1

Augereau, J. C., Nelson, R. P., Lagrange, A. M., Papaloizou, J. C. B., & Mouillet, D. 2001, Astronomy and Astrophysics, 370, 447

Aumann, H. H. et al. 1984, Astrophysical Journal, Letters to the Editor, 278, L23

Backman, D. E., Dasgupta, A., & Stencel, R. E. 1995, Astrophysical Journal, Letters to the Editor, 450, L35+

Backman, D. E. & Paresce, F. 1993, in Protostars and Planets III, ed. E. H. Levy & J. I. Lunine, 1253–1304

Balona, L. A. et al. 1996, Monthly Notices of the RAS, 281, 1315

Balona, L. A., Krisciunas, K., & Cousins, A. W. J. 1994, Monthly Notices of the RAS, 270, 905

Bate, M. R., Bonnell, I. A., & Bromm, V. 2003, Monthly Notices of the RAS, 339, 577

Beckwith, S. V. W., Henning, T., & Nakagawa, Y. 2000, Protostars and Planets IV, 533

Beckwith, S. V. W., Sargent, A. I., Chini, R. S., & Guesten, R. 1990, Astronomical Journal, 99, 924

Beichman, C. A., Neugebauer, G., Habing, H. J., Clegg, P. E., & Chester, T. J., eds. 1988, Infrared astronomical satellite (IRAS) catalogs and atlases. Volume 1: Explanatory supplement, Vol. 1

Booth, M., Wyatt, M. C., Morbidelli, A., Moro-Martín, A., & Levison, H. F. 2009, Monthly Notices of the RAS, 399, 385

Booth et al., M. 2012, in prep.

Briceño, C., Luhman, K. L., Hartmann, L., Stauffer, J. R., & Kirkpatrick, J. D. 2002, Astrophysical Journal, 580, 317

Brott, I. & Hauschildt, P. H. 2005, in ESA Special Publication, Vol. 576, The Three-Dimensional Universe with Gaia, ed. C. Turon, K. S. O'Flaherty, & M. A. C. Perryman, 565–+

Brown, J. M. et al. 2007, Astrophysical Journal, Letters to the Editor, 664, L107

Burns, J. A., Lamy, P. L., & Soter, S. 1979, Icarus, 40, 1

Chen, C. H., Fitzgerald, M. P., & Smith, P. S. 2008, Astrophysical Journal, 689, 539

Chen et al., C. H. 2006, Astrophysical Journal, Supplement Series, 166, 351

Chun, M. et al. 2008, in Society of Photo-Optical Instrumentation Engineers (SPIE) Conference Series, Vol. 7015, Society of Photo-Optical Instrumentation Engineers (SPIE) Conference Series

Churcher, L. J. et al. 2011, Monthly Notices of the RAS, 1596

Cousins, A. W. J. & Warren, P. R. 1963, Monthly Notes of the Astronomical Society of South Africa, 22, 65

Cutri et al., R. M. et al. 2003, 2MASS All Sky Catalog of point sources., ed. Cutri, R. M., Skrutskie, M. F., van Dyk, S., Beichman, C. A., Carpenter, J. M., Chester, T., Cambresy, L., Evans, T., Fowler, J., Gizis, J., Howard, E., Huchra, J., Jarrett, T., Kopan, E. L., Kirkpatrick, J. D., Light, R. M., Marsh, K. A., McCallon, H., Schneider, S., Stiening, R., Sykes, M., Weinberg, M., Wheaton, W. A., Wheelock, S., & Zacarias, N.

De Cat et al., P. 2006, Astronomy and Astrophysics, 449, 281

de Graauw et al. 2010, Astronomy and Astrophysics, 518, L6+

Dent, W. R. F., Walker, H. J., Holland, W. S., & Greaves, J. S. 2000, Monthly Notices of the RAS, 314, 702

Dobashi, K. 2011, Publications of the ASJ, 63, 1

Draper, P. W. et al. 2005, in Astronomical Society of the Pacific Conference Series, Vol. 347, Astronomical Data Analysis Software and Systems XIV, ed. P. Shopbell, M. Britton, & R. Ebert, 22–+

Dullemond, C. P., Hollenbach, D., Kamp, I., & D'Alessio, P. 2007, Protostars and Planets V, 555

Eiroa, C. et al. 2010, Astronomy and Astrophysics, 518, L131+

Ertel, S. et al. 2011, Astronomy and Astrophysics, 533, A132+

Evans, N. J. et al. 2009, Astrophysical Journal, Supplement Series, 181, 321

Gray et al., R. O. 2006, Astronomical Journal, 132, 161

Greaves, J. S. et al. 1998, Astrophysical Journal, Letters to the Editor, 506, L133

— 2005, Astrophysical Journal, Letters to the Editor, 619, L187

Griffin, M. J. et al. 2010, Astronomy and Astrophysics, 518, L3+

Hartmann, L. 1998, Accretion Processes in Star Formation, ed. Hartmann, L.

Hartmann et al. 2005, Astrophysical Journal, 629, 881

Høg et al., E. 2000, Astronomy and Astrophysics, 355, L27

Holland, W. S. et al. 1999, Monthly Notices of the RAS, 303, 659

Hughes, A. M. et al. 2010, Astronomical Journal, 140, 887

Ishihara, D. et al. 2010, Astronomy and Astrophysics, 514, A1+

Jayawardhana, R., Ardila, D. R., Stelzer, B., & Haisch, Jr., K. E. 2003, Astronomical Journal, 126, 1515

Jayawardhana, R., Mohanty, S., & Basri, G. 2005, Mem. Soc. Astron. Italiana, 76, 295

Jenness, T., Cavanagh, B., Economou, F., & Berry, D. S. 2008, in Astronomical Society of the Pacific Conference Series, Vol. 394, Astronomical Data Analysis Software and Systems XVII, ed. R. W. Argyle, P. S. Bunclark, & J. R. Lewis, 565–+

Jenness, T. & Lightfoot, J. F. 1998, in Astronomical Society of the Pacific Conference Series, Vol. 145, Astronomical Data Analysis Software and Systems VII, ed. R. Albrecht, R. N. Hook, & H. A. Bushouse, 216–+

Jenness, T., Lightfoot, J. F., & Holland, W. S. 1998, in Society of Photo-Optical Instrumentation Engineers (SPIE) Conference Series, Vol. 3357, Society of Photo-Optical Instrumentation Engineers (SPIE) Conference Series, ed. T. G. Phillips, 548–558

Jewitt, D. C. & Luu, J. X. 1995, Astronomical Journal, 109, 1867

Kalas, P. et al. 2008, Science, 322, 1345

Kalas, P., Graham, J. R., & Clampin, M. 2005, Nature, 435, 1067

Kaye, A. B., Handler, G., Krisciunas, K., Poretti, E., & Zerbi, F. M. 1999, Publications of the ASP, 111, 840

Kennedy et al., G. 2012, in prep.

Kenyon, S. J. & Bromley, B. C. 2004, Astronomical Journal, 127, 513

— 2008, Astrophysical Journal, Supplement Series, 179, 451

Kenyon, S. J., Dobrzycka, D., & Hartmann, L. 1994, Astronomical Journal, 108, 1872

Kim et al. 2006, Astrophysical Journal, Supplement Series, 162, 161

Klapper, G., Lewen, F., Gendriesch, R., Belov, S., & Winnewisser, G. 2000, Journal of Molecular Spectroscopy, 201, 124

— 2001, Naturforsch, 56a, 329

Kraus, A. L. & Hillenbrand, L. A. 2009, Astrophysical Journal, 704, 531

Kraus, A. L., White, R. J., & Hillenbrand, L. A. 2006, Astrophysical Journal, 649, 306

Krivov, A. V. 2010, Research in Astronomy and Astrophysics, 10, 383

Lagrange, A.-M. et al. 2010, Science, 329, 57

— 2009, Astronomy and Astrophysics, 493, L21

Laor, A. & Draine, B. T. 1993, Astrophysical Journal, 402, 441

Lawler et al., S. M. 2009, Astrophysical Journal, 705, 89

Levison, H. F., Morbidelli, A., Vanlaerhoven, C., Gomes, R., & Tsiganis, K. 2008, Icarus, 196, 258

Liseau, R. et al. 2010, Astronomy and Astrophysics, 518, L132+

Liu, M. C. et al. 2010, in Society of Photo-Optical Instrumentation Engineers (SPIE) Conference Series, Vol. 7736, Society of Photo-Optical Instrumentation Engineers (SPIE) Conference Series

Luhman, K. L., Allen, P. R., Espaillat, C., Hartmann, L., & Calvet, N. 2010, Astrophysical Journal, Supplement Series, 186, 111

Marshall, J. P. et al. 2011, Astronomy and Astrophysics, 529, A117+

Matthews, B. C., Kalas, P. G., & Wyatt, M. C. 2007, Astrophysical Journal, 663, 1103

Matthews et al., B. C. 2010, Astronomy and Astrophysics, 518, L135+

— 2012, in prep.

Mermilliod, J. C. 2006, VizieR Online Data Catalog, 2168, 0

Mohanty, S., Jayawardhana, R., & Basri, G. 2005, Astrophysical Journal, 626, 498

Moshir, M. & et al. 1990, in IRAS Faint Source Catalogue, version 2.0 (1990), 0–+

Mouillet, D., Lagrange, A. M., Augereau, J. C., & Ménard, F. 2001, Astronomy and Astrophysics, 372, L61

Mouillet, D., Larwood, J. D., Papaloizou, J. C. B., & Lagrange, A. M. 1997, Monthly Notices of the RAS, 292, 896

Najita, J. & Williams, J. P. 2005, Astrophysical Journal, 635, 625

Ott, S. 2010, in Astronomical Society of the Pacific Conference Series, Vol. 434, Astronomical Data Analysis Software and Systems XIX, ed. Y. Mizumoto, K.-I. Morita, & M. Ohishi, 139–+

Padoan, P. & Nordlund, Å. 2004, Astrophysical Journal, 617, 559

Parker, A. H., Kavelaars, J., Petit, J.-M., Jones, L., Gladman, B., & Parker, J. 2011, ArXiv e-prints

Perryman, M. A. C. & ESA, eds. 1997, ESA Special Publication, Vol. 1200, The HIPPARCOS and TYCHO catalogues. Astrometric and photometric star catalogues derived from the ESA HIPPARCOS Space Astrometry Mission

Phillips et al. 2010, Monthly Notices of the RAS, 403, 1089

Pilbratt et al., G. L. 2010, Astronomy and Astrophysics, 518, L1+

Plavchan, P., Jura, M., & Lipscy, S. J. 2005, Astrophysical Journal, 631, 1161

Poglitsch et al., A. 2010, Astronomy and Astrophysics, 518, L2+

Pontoppidan, K. M., Blake, G. A., van Dishoeck, E. F., Smette, A., Ireland, M. J., & Brown, J. 2008, Astrophysical Journal, 684, 1323

Quillen, A. C. 2006, Monthly Notices of the RAS, 372, L14

Reidemeister, M., Krivov, A. V., Stark, C. C., Augereau, J.-C., Löhne, T., & Müller, S. 2011, Astronomy and Astrophysics, 527, A57+

Reipurth, B. & Clarke, C. 2001, Astronomical Journal, 122, 432

Rhee, J. H., Song, I., Zuckerman, B., & McElwain, M. 2007, Astrophysical Journal, 660, 1556

Rieke, G. H. et al. 2004, Astrophysical Journal, Supplement Series, 154, 25

Schaller, G., Schaerer, D., Meynet, G., & Maeder, A. 1992, Astronomy and Astrophysics, Supplement Series, 96, 269

Schneider, G. et al. 2006, Astrophysical Journal, 650, 414

Scholz, A., Jayawardhana, R., & Wood, K. 2006, Astrophysical Journal, 645, 1498

Shu, F. H., Adams, F. C., & Lizano, S. 1987, Annual Review of Astronomy and Astrophysics, 25, 23

Sibthorpe et al., B. 2010, Astronomy and Astrophysics, 518, L130+

— 2012, in prep.

Strom, K. M., Strom, S. E., Edwards, S., Cabrit, S., & Skrutskie, M. F. 1989, Astronomical Journal, 97, 1451

Su, K. Y. L. et al. 2009, Astrophysical Journal, 705, 314

Thureau et al., N. 2012, in prep.

van Leeuwen, F. 2007, Astronomy and Astrophysics, 474, 653

Watson, A. M., Stapelfeldt, K. R., Wood, K., & Ménard, F. 2007, Protostars and Planets V, 523

Williams, J. P. & Andrews, S. M. 2006, Astrophysical Journal, 653, 1480

Wyatt, M. C. 2003, Astrophysical Journal, 598, 1321

— 2008, Annual Review of Astronomy and Astrophysics, 46, 339

Wyatt, M. C., Smith, R., Greaves, J. S., Beichman, C. A., Bryden, G., & Lisse, C. M. 2007, Astrophysical Journal, 658, 569

Zhu, L., Yang, J., & Wang, M. 2007, CAA, 31, 387

Appendix A

Appendix: Background sources

Because our observations are ∼3 times and ∼2 times the background confusion limit at 100 and 160 μm, respectively (Matthews et al., 2012, in prep.), we must examine the maps for nearby background sources. There is a ∼12% and ∼8% probability of finding a 5 - 15 mJy nearby source within 20″ of the target at 100 and 160 μm, respectively, in DEBRIS maps (Thureau et al., 2012, in prep.). It is important to identify and characterize nearby sources visible at PACS wavelengths in order to facilitate the analysis of these sources at the longer SPIRE wavelengths, where it is more difficult to isolate the disk emission. Additionally, we must consider the possibility that nearby sources are contributing to the flux measured by other observatories (e.g., *Spitzer* and *IRAS*). For example, Rhee et al. (2007) regard the *IRAS* 60 μm flux of γ Dor with caution because of a nearby optical source about 70″ away. A source at this distance would be indistinguishable from γ Dor with *IRAS* because of its large beam size (see Table 1.2).

There are no nearby background sources within 2′ of γ Dor listed in the NASA/IPAC Extragalactic Database (NED) or within 40″ in the NASA/IPAC Infrared Science Archive. The nearest source resolved by SIMBAD is ∼320″ away. Therefore we must rely on identifying sources based our *Herschel* maps. We do so by fitting a significant PSF to a source's emission and finding its position to be consistent between the 100 and 160 μm maps. We also examine various combinations of the four scan maps (shown in Figure A.1 and A.2) used to produce the maps in Figure 3.3 to determine which features are real. From this criteria we are only able to identify one nearby source that lies about 30″ to the south-east of the peak of γ Dor's emission.

The background source is fit with a PSF (with the same fitting procedure described in Section 4.2.1) in the PACS maps to determine its flux and position. (The

Table A.1. A potential background source

Band (μm)	Flux (mJy)
70	11.4 ± 1.6
100	20.0 ± 1.9
160	35.0 ± 5.4
250	28.0 ± 5.7
350	18.5 ± 7.9[a]
500	<16.7 ± 5.9[b]

[a]Only a 2.5 σ detection.

[b]A 3 σ detection, however, the γ Dor system is also contributing to this flux.

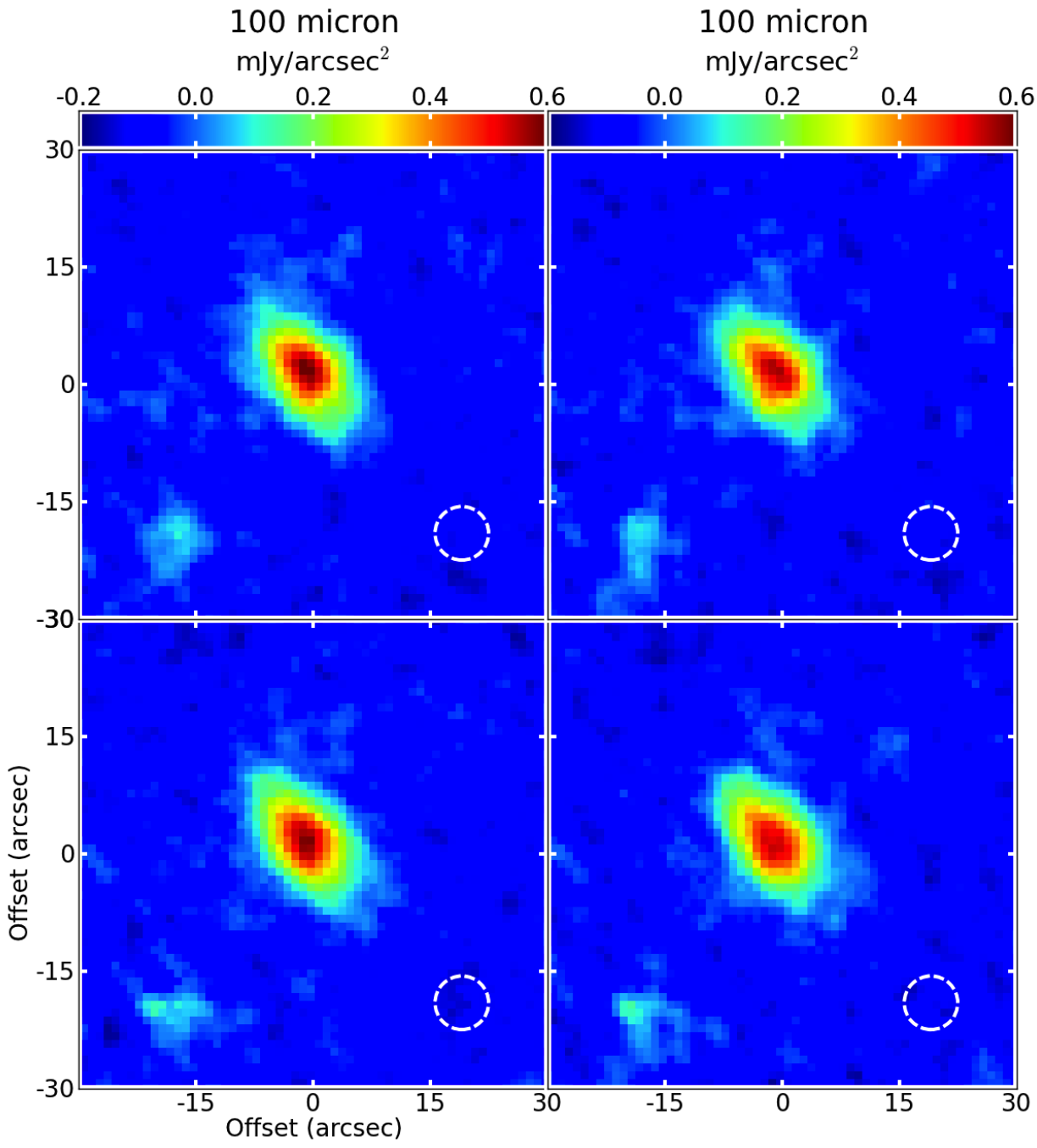

Figure A.1 The four combinations of the four scans taken in the observation of γ Dor at 100 μm. The south-east background source is consistent in each of these. No other background source can be identified. The beam sizes are shown in the bottom right corners.

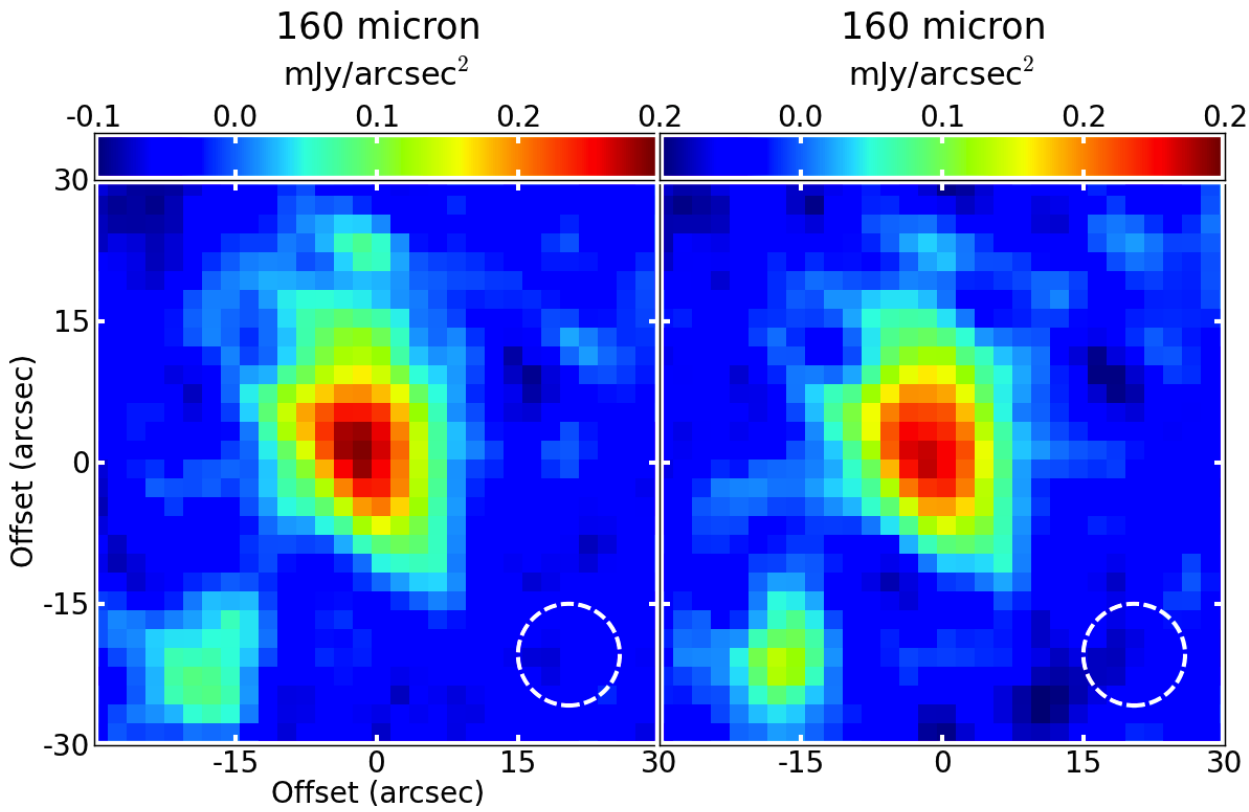

Figure A.2 Two combinations of the four scans taken in the observation of γ Dor at 160 μm. The south-east background source is consistent in each of these. No other background source can be identified. The beam sizes are shown in the bottom right corners.

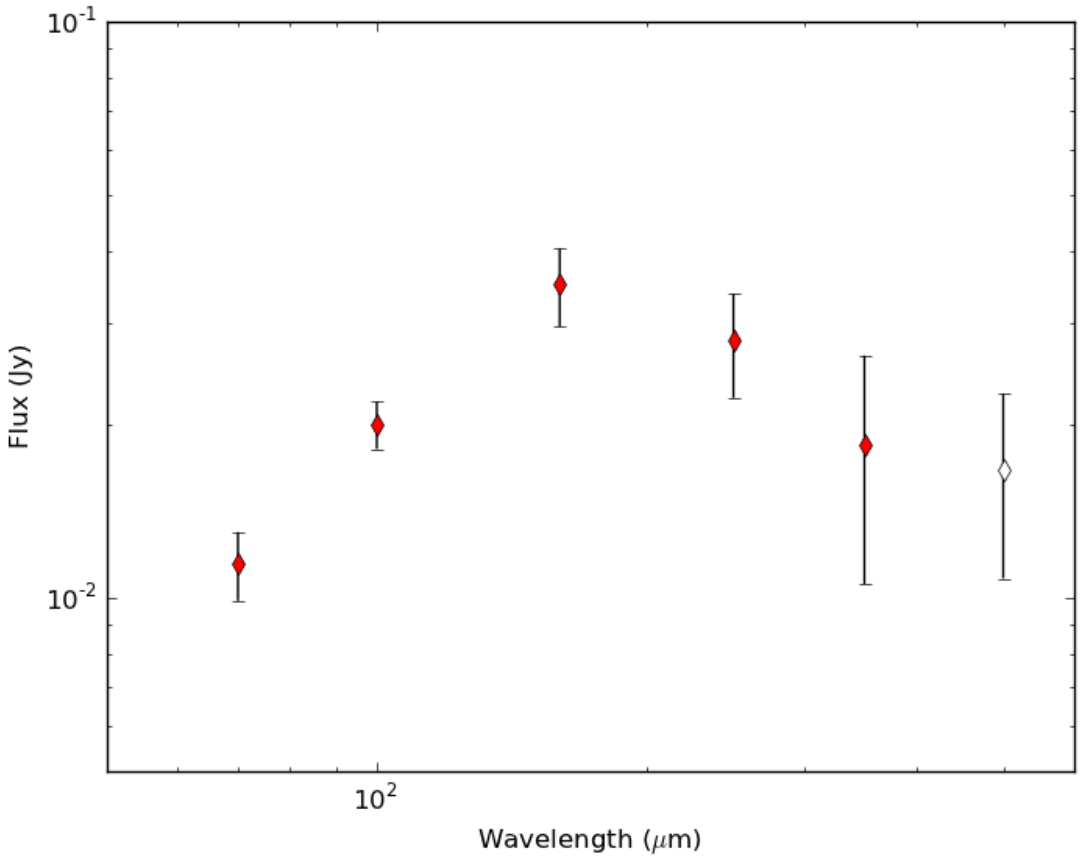

Figure A.3 The SED for the south-east background source. Error bars include errors in the PSF fits, noise, pixel size correction factors, and calibration errors. The 500 μm flux point is shown with an open symbol because it includes flux from the γ Dor system.

background source is also modelled with 2D Gaussians, as described in Section 4.2.4, but these tended towards a more extended Gaussian due to the noise from the surroundings.) The coordinates measured at 160 μm are used to fix those at SPIRE wavelengths where two PSFs must be fit simultaneously to the background source and γ Dor because of the decreasing resolution. (This is evident when viewing the maps in Figure 3.3.) The fluxes of the fitted PSFs are listed in Table A.1. The flux measured at 350 μm is only 2.5 σ with respect to the noise measured in the map. A single PSF is fit at 500 μm because the background source and γ Dor cannot be separated. Although the flux of this fitted PSF is 3 σ, the result is quoted as an upper limit since γ Dor is also contributing to it. The SED of the background source, using *Herschel* fluxes is shown in Figure A.3. The fitted PSF can be subtracted from the maps in order to generate a clearer image of γ Dor's disk as shown in the bottom panels of Figure 3.3.